Funded by the
European Union

ICE GENESIS

Creating the next generation of 3D simulation means for icing

Type of action: Research and Innovation Action

Call identifier: H2020-MG-2018-SingleStage

Topic: MG-2-5-2018 Innovative technologies for improving aviation safety and certification in icing conditions

---

Deliverable D6.4

Report on FZDZ calibration for each IWT involved in the project

EC Grant Agreement number: **824310**

Start date of project: 1 January 2019 Duration: 60 months

Lead beneficiary of this deliverable: CIRA

Due date of deliverable: 30/04/2022 Actual submission date: 28/03/2024

Version #: R1.0

Project funded by the European Commission within the H2020 Programme (2014-2020)		
Type		
R	Document, report excluding the periodic and final reports	X
DEM	Demonstrator, pilot, prototype	
DEC	Websites, patents filing, press & media actions, videos, etc.	
OTHER	Software, technical diagram, etc.	
ETHICS	Ethics requirement	
ORDP	Open Research Data Pilot	
Dissemination level		
PU	PUBLIC, fully open, no embargo e.g. web	
PU+E1	PUBLIC after embargo of 12 months from date of publication	
PU+E3	PUBLIC after embargo of 3 years after the project’s end	
RE	RESTRICTED, only for certain members of the consortium (including the Commission Services)	
CO	CONFIDENTIAL, only for members of the consortium (including the Commission Services)	X
CO+IGAB	CONFIDENTIAL, only for members of the consortium (including the Commission Services) and for the ICE GENESIS Advisory Board	

Revision History

V #	Date	Description / Reason of change	Author
0.1	22/03/2024	First Version	B. Esposito (CIRA), W. Breitfuß (RTA)
0.2	27/03/2024	Version with reviewer comments	B. Esposito (CIRA), W. Breitfuß (RTA)
1.0	28/03/2024	Final Version	B. Esposito (CIRA), W. Breitfuß (RTA)

Deliverable Contributors

Authors

Organisation	Authors' name	Export control status date	Export control status
RTA	Wolfgang Breitfuß	19/03/2024	No data subject to export control
CIRA	Biagio Esposito	19/03/2024	No data subject to export control

Contributors

Organisation	Authors' name	Export control status date	Export control status
DLR	Romy Heller	19/03/2024	No data subject to export control
RV	Sawitree Saengkaew	19/03/2024	No data subject to export control

Export Control Status

Author / Contributor	Type of data	Position in document of concerned text/data*	Jurisdiction and ECCN under this jurisdiction	Status of authorization
CIRA	Experimental data, Computational data	§5	No data subject to export control	Not Applicable
DLR	Experimental data	§4.4.6, 4.4.7, 5.3	No data subject to export control	Not Applicable
RV	Experimental data	§4.4.8, 5.4.2	No data subject to export control	Not Applicable
RTA	Experimental data, Computational data	§ 4	No data subject to export control	Not Applicable

Internal Reviewers

Organisation	Internal Reviewers' name
Dassault	Francois Caminade
Airbus	Olivier Blesbois

Table of Contents

Table of Tables

Table of Figures

1 Glossary

Abbreviation / Acronym	Description/meaning
2D-C	Optical Array Probe
CCP	Cloud Combination Probe
CDP	Cloud Droplet Probe
CIP	Cloud Imaging Probe
FSSP	Forward Scattering Spectrometer Probe
FZDZ	Freezing Drizzle
FZRA	Freezing Rain
LSI	Laser Sheet Imaging
LWC	Liquid Water Content
MVD	Median Volumetric Diameter
MW	Multi-Wire probe
PMS	Particle Measuring Systems
PSD	Particle Size Distribution
RP	Robust Probe
RR	Rosin-Rammler distributions
SAT	Static Air Temperature
SBS	Spray Bar System
SLD	Supercooled Large Droplet
SLD	Supercooled Large Droplet
TRL	Technology Readiness Level
TWC	Total Water Content
ZLE	Freezing Drizzle

2 Executive Summary

This deliverable provides the results from the measurements and calibration activities performed in the RTA Icing Wind Tunnel (IWT) and a summary of the measurement activities executed at CIRA-IWT, showing a preliminary calibration.

A full assessment and calibration of the FZDZ capabilities for RTA-IWT has been presented in this report, showing the main steps accomplished to achieve the Facility Technology Readiness Level TRL 5 in the project. The guidelines on the procedures to be followed for the cloud characterizations have been defined in deliverable D6.1-2, "Proposal of Calibration Instruments and Procedures for FZDZ and FZRA". Three separate test campaigns, starting in August 2019 and ending in June 2021, were conducted at RTA, whose SLD capabilities were already available at the start of the project, limited to PSD/MVD calibration for the FZDZ. During the project period, a better assessment of the LWC and a review of the PSD/MVD envelope for both FZDZ and FZRA were performed using selected instrumentation by Deliverable D6.1-2 to achieve a better accuracy of LWCs characterization. Moreover, a refinement of PSD/MVD, cloud uniformity as well as droplet temperature measurements were performed and presented in this report outlining the RTA-IWT calibration for Freezing Drizzle with an MVD of less and more than 40 µm.

After the upgrade with a new spray nozzle, followed by the commissioning of the spray bar system in January-February 2022, the measurements in the CIRA-IWT were planned to a single slot from April 2022 to early June 2022. The calibration began with the cloud uniformity check and extended to LWC and PSD/MVD measurements for one of the four spray bar configurations. The time available only allowed to characterize cloud conditions at the sea level for FZDZ higher and lower than 40 µm, with few conditions for checking different pressure altitudes and spray bar configurations. This report shows the preliminary performance of CIRA-IWT for SLD conditions, as not enough measuring points were relatable to support valid statistical data analysis to determine general calibration curves for MVD/PSD to correlate with LWCs data.

3 Introduction

The ambition of the ICE GENESIS project is to improve the experimental test capabilities of icing facilities to generate or reproduce representative Supercooled Large Droplet (SLD) conditions and to define a common calibration methodology. At the beginning of the program, six wind tunnel owners were involved in the ICE-GENESIS Work Package 6 (SLD Test Capability), CIRA, MINDEF, RTA, TUBS, TSAGI, and CIAM. However, the partnership with TSAGI and CIAM was terminated for geopolitical reasons in 2022. Moreover, MINDEF also discontinued its activities in ICE-GENESIS. Therefore, concerning the original target, this report is limited to providing the results of the measurements supporting the calibration activities for Appendix O Freezing Drizzle (FZDZ) conditions only for the RTA-IWT and the CIRA-IWT.

4 RTA Icing Wind Tunnel

4.1 Test Setup

All of the tests and measurements mentioned in this report were performed in the large IWT using the high-speed configuration with the additional contraction nozzle, a schematic is shown in Figure 1. The test section area indicated in the schematic shows the calibrated area for Appendix C icing clouds. This setup enables test section airspeeds between 20 m/s and 80 m/s and offer the benefit of a low contraction ratio, which minimizes potential secondary droplet breakup. Furthermore, the asymmetric contraction nozzle also proved to be beneficial for the generation and transport of large rain droplets.

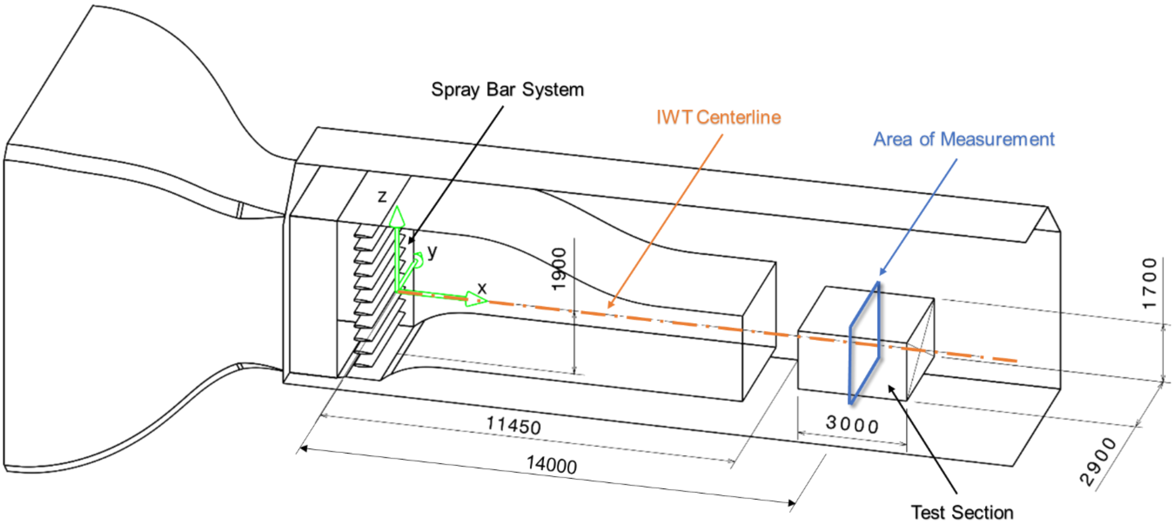

Figure 1: Schematic of the RTA IWT "high-speed configuration"

RTA's spray bar system features eleven spray bars with 24 spray nozzles each. The 24 nozzles of each spray bar are split into two separately controllable circuits, where every second nozzle belongs to circuit 1 and every other nozzle to circuit 2. The supply water- and air-pressures as well as the water supply temperature can be controlled independently for those two circuits, which enables the generation of bimodal Particle Size Distributions (PSDs) The large particles can be injected with precooled water, whereas the particles of the small mode can be supplied with pre-heated water in order to prevent freeze-out. The distance of about 11.5 m from the injection to the test section should provide sufficient time for the large droplets to reach a supercooled state.

4.2 Feasibility Study

A feasibility study was performed to investigate the potential of generating FZDZ and FZRA conditions in RTA's IWT by means of spray nozzle assessments using a nozzle test rig, numerical simulations and preliminary tests in the IWT. These investigations were performed prior to the ICE GENESIS project and therefore are just summarised briefly in this report.

4.2.1 Particle Trajectories and Secondary Droplet Breakup

The particle trajectories at different test section airspeeds were analysed using numerical simulation tools. The injection velocities of the particles were measured using a high-speed camera and used as an input for the simulations. The analysis revealed that for FZRA conditions a minimum test section airspeed of 40 m/s to 45 m/s is required as the gravitational influence of the large rain droplets significantly affects the trajectories at low speeds. The results also showed that only certain spray bars can be used, as some of the large particles impinge on the additional contraction nozzle before reaching the test section. Example results for droplets with diameters between 100 µm and 1200 µm can be found in Figure 2.

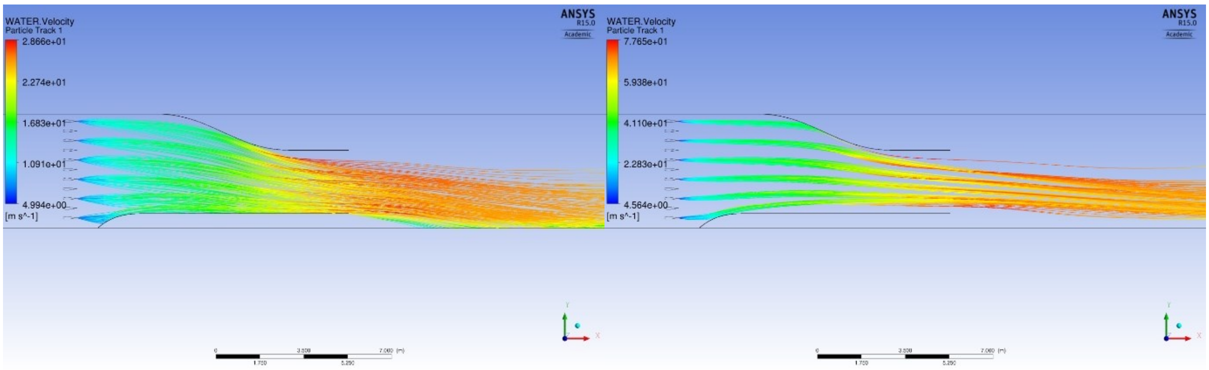

Figure 2: Example particle tracks (100 µm – 1200 µm) for the RTA IWT at a test section airspeed of 30 m/s (left) and 80 m/s (right)

Furthermore, potential secondary droplet breakup was analysed using the so-called Weber number. The critical Weber number for when breakup starts to occur varies between 11-14 [3]. Simulations with and without a droplet deformation model were performed. For the runs with deformation the same approach NASA used to investigate breakup in Glenn Icing Research Tunnel (IRT) was used [4]. The Droplet deformation is based on a modified Bond number from [5] and the drag of the deformed droplet was taken from [6]. The simulations have shown that droplets with diameters of up to about 1500 µm can be transported to the test section at the maximum airspeed without exceeding a Weber number of 14, when the deformed droplet model is used. This can mainly be attributed to the low contraction ratio (1.84) of the additional contraction nozzle. In Figure 3 and Figure 4 an example evaluation for a large FZDZ droplet with a diameter of 500 µm is shown for the maximum airspeed of 80 m/s where the solid lines show the fully spherical model, and the dashed lines show the results using the droplet deformation model. A maximum Weber Number of less than 3 is reached in the main contraction zone of the additional contraction nozzle, where the flow is accelerated the most. Running the simulation with or without the deformation model did not have a significant effect on the result. In the test section the droplet is about 9% slower compared to the ambient airspeed and has a trajectory angle within less than 1.3° compared to a droplet falling with its terminal velocity at an airspeed of 80 m/s. Droplet breakup is no issue for FZDZ over the full airspeed range.

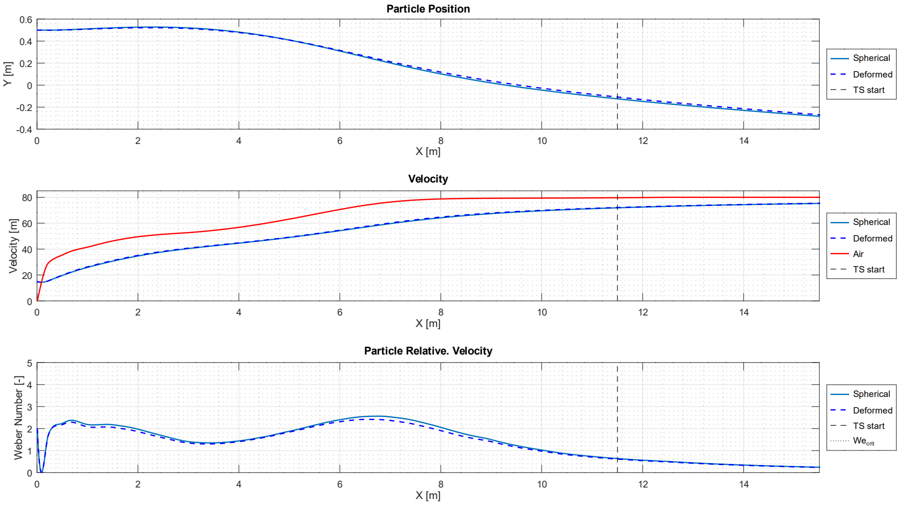

Figure 3: Example secondary droplet breakup analysis for a 500 µm droplet in the RTA IWT at 80 m/s (dashed line = with droplet deformation, solid line = spherical model)

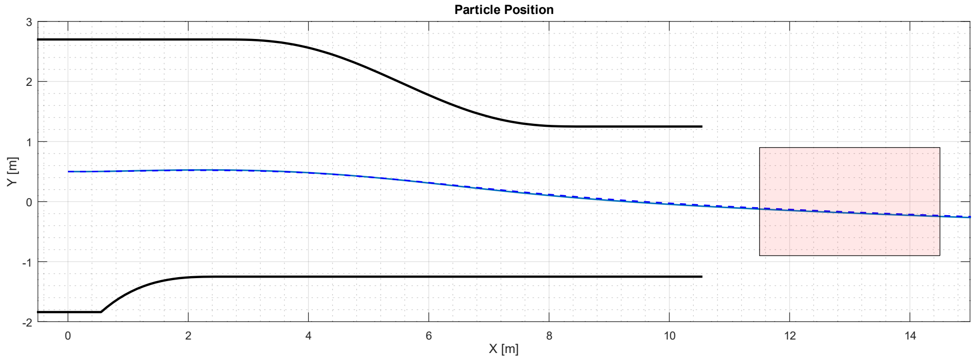

Figure 4: Example trajectory of a 500 µm droplet in the RTA IWT at 80 m/s (dashed line = with droplet deformation, solid line = spherical model)

4.2.2 Droplet Temperature

The achievable droplet temperatures in the test section were also investigated by means of numerical and analytical simulations using the model described in [7]. The results for a FZDZ MVD > 40 µm condition at a static test section air temperature of -5°C and a test section airspeed of 60 m/s are shown in Figure 5. The increased thermal inertia of the droplets from the SLD spectrum causes a shallow cool down behaviour and therefore requires pre-cooled water at considerable low temperatures. The injection temperature of the droplets was set to 5°C. All droplets of the considered diameter spectrum cool down at least to freezing temperature before reaching the test section. The mass averaged temperature for the particles of the large mode is about -4.1°C at the start of the test section according to the simulations (Figure 6). For very large rain droplets with diameters of more than 1 mm, colder ambient temperatures (< -10°C) and / or colder supply temperatures might be required to achieve a supercooled state.

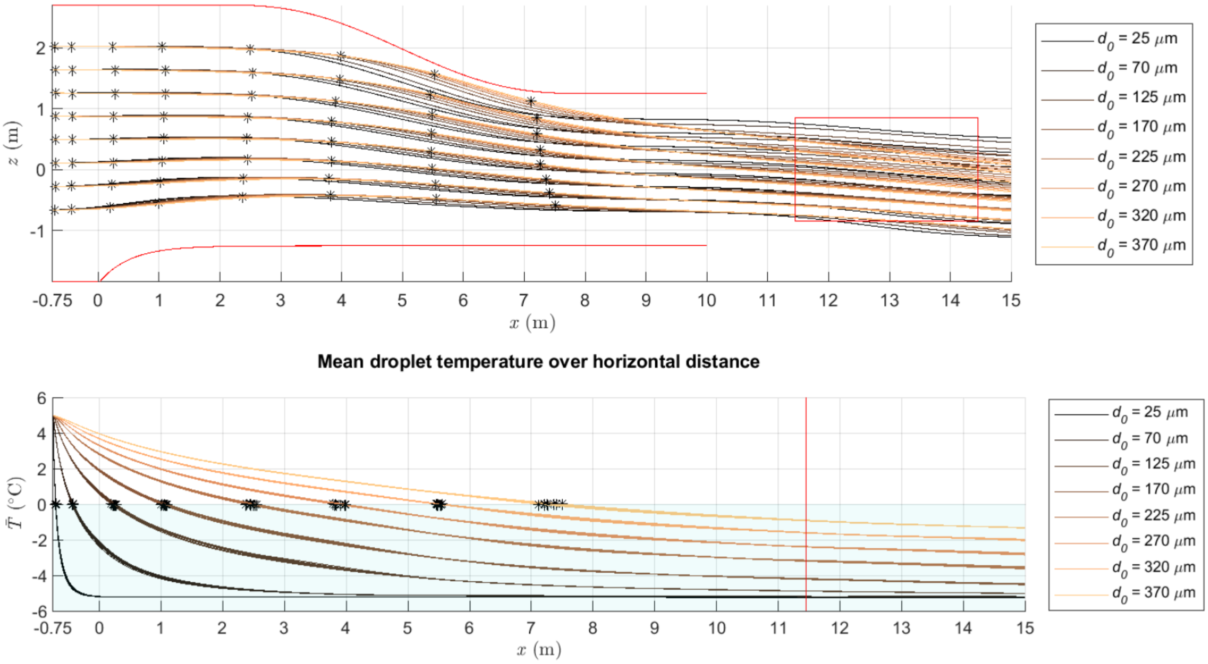

Figure 5: Results for a FZDZ icing cloud simulation in the RTA IWT, the asterisks mark the position where the droplet reaches a supercooled state

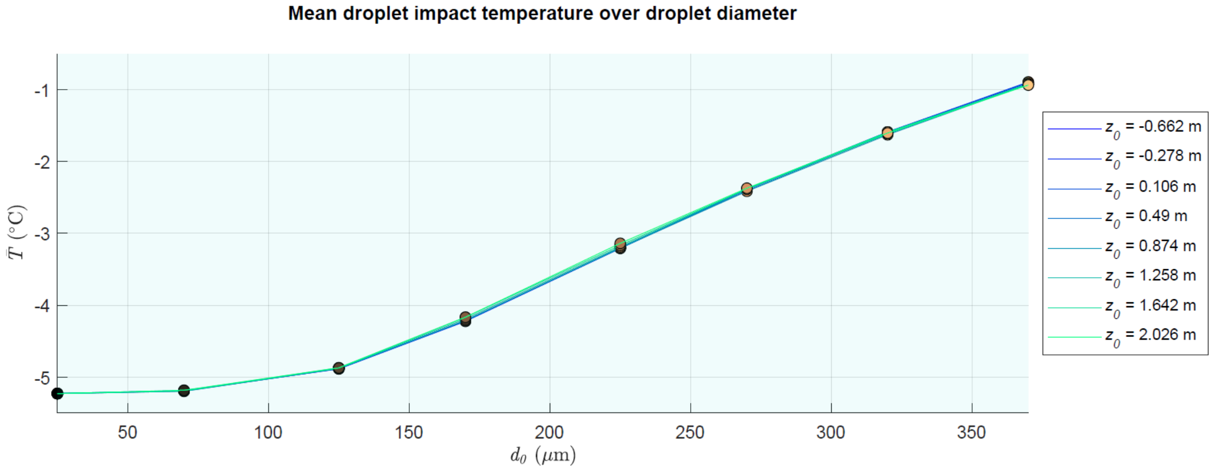

Figure 6: Mean droplet temperature at the start of the test section (11.5m) in the RTA IWT at 60 m/s and static test section air temperature of -5°C.

4.3 Freezing Drizzle MVD < 40 µm

For Freezing Drizzle (FZDZ) with a Median Volume Diameter (MVD) of smaller than 40 µm, MVD, Particle size distribution (PSD) and Liquid Water Content (LWC) investigations have been performed during internal, nationally funded (“FFG Aviation Icing Tests II-IV”) and internationally funded (“ICE GENESIS”) research projects. The Requirements on the PSD and the LWC range is shown in Figure 7.

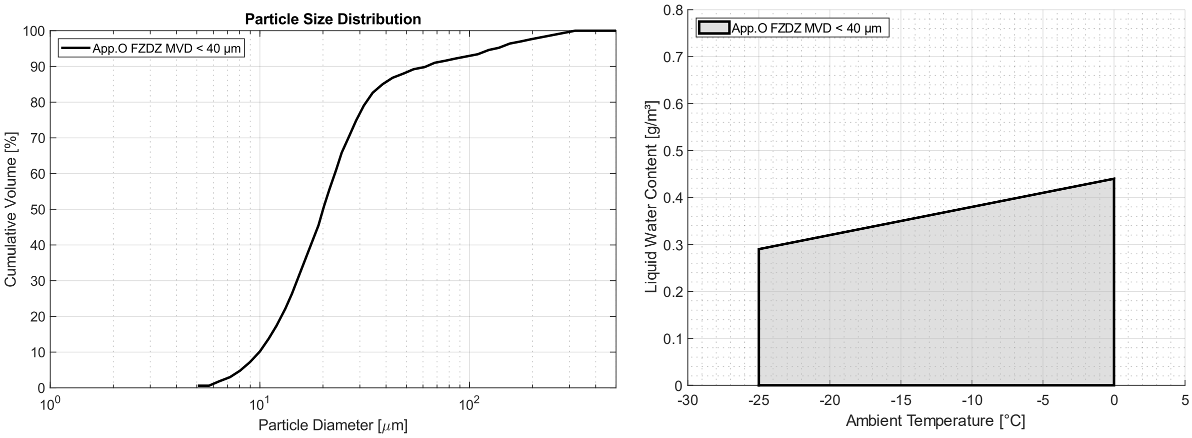

Figure 7: Appendix O Freezing Drizzle MVD < 40 µm PSD (left) and LWC range (right)

According to Cober and Isaac [1, p. 271] the MVD of FZDZ MVD < 40 µm conditions should be in the range of 20 µm with a maximum diameter of 389 µm. Figure 8 shows the individual measured PSDs and the average cumulative mass spectrum [2]. The 99.0% LWC of all cloud measurements was 0.44 g/m³, which is used as the upper limit in Appendix O, the maximum observed LWC was 0.77 g/m³ [1, pp. 278-280].

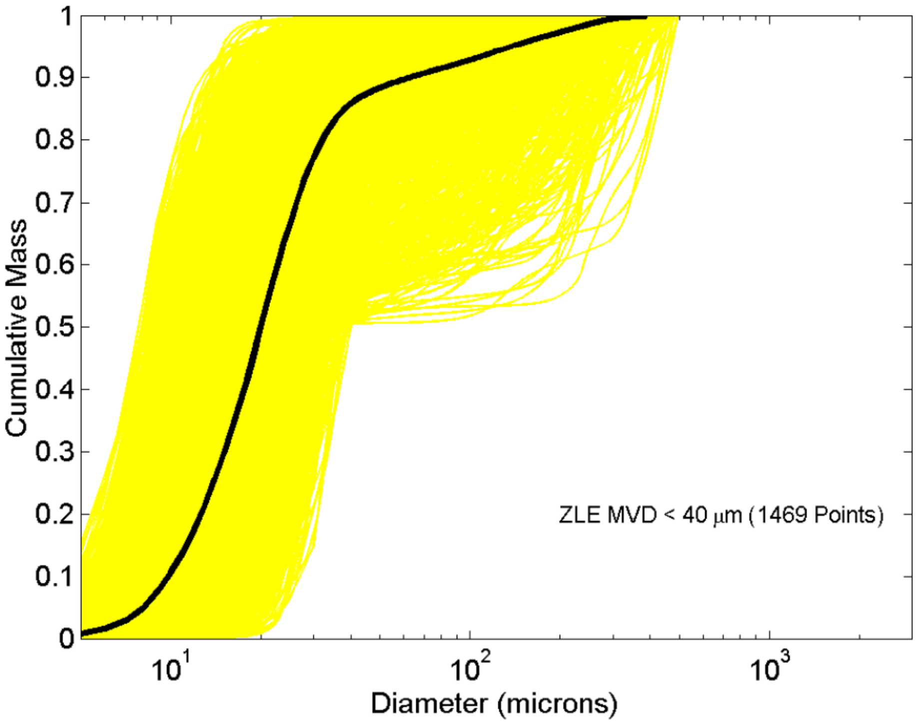

Figure 8: Average Cumulative Mass Spectrum for FZDZ MVD < 40 µm compared to each individual cumulative mass spectra [2, p.43]

Table 1 lists the four settings which have been investigated in the RTA IWT. Due to the very small amount of required large particles, it was not possible to inject a bimodal distribution close to the requirements, while still achieving low LWCs. Monomodal distributions which also include larger particles were investigated. The “long tail” in the PSDs is created by very low water supply pressures to the atomizing spray nozzles, which are also used for Appendix C cloud generation.

Table 1: Investigated Spray bar settings for FZDZ MVD < 40 µm conditions

Setting	p_{water} 1 [bar]	p_{air} 1 [bar]	p_{water} 2 [bar]	p_{air} 2 [bar]
FZDZ S1	0.40	0.96	0.40	0.96
FZDZ S2	0.30	0.84	0.30	0.84
FZDZ S3	0.20	0.72	0.20	0.72
FZDZ S4	0.15	0.62	0.15	0.62

4.3.1 MVD / PSD Measurements

The MVDs and PSDs of the settings mentioned in Table 1 were measured using the Malvern Spraytec instrumentation with the 300 mm lens assembly and / or the CAPS probe from Droplet Measurement Technologies. Table 2 lists the resulting MVDs. The detailed PSDs are shown in Section 4.3.3.

Table 2: MVD / PSD Measurements for FZDZ MVD < 40 µm conditions

Setting	Instrument	TAS [m/s]	SAT [°C]	MVD [µm]	Year
FZDZ S1	MalvernSpraytec	20	2	18.1	2017
FZDZ S2	MalvernSpraytec	20	2	18.4	2017
FZDZ S3	MalvernSpraytec	20	2	19.8	2017
FZDZ S1	MalvernSpraytec	20	2	22.3	2020
FZDZ S2	MalvernSpraytec	20	2	22.9	2020
FZDZ S3	CAPS	60	2	23.7	2020
FZDZ S4	CAPS	60	2	26.1	2020

4.3.2 MVD Calibration

As the pressure ranges for the FZDZ MVD < 40 µm settings are within the standard MVD calibration curves of the atomizing spray nozzles (based on calibration measurements in 2020), this calibration curve (Equation 1) is used to calculate the MVD. Figure 9 shows the relevant section of the calibration curve. Figure 10 shows a comparison of the calibrated and measured MVDs. Overall, the standard calibration curve does give a good approximation of the measured MVD, the largest deviation is seen for some of the older measurement data which were performed before the cloud uniformity was improved.

$$MVD_s = \exp(5.391 - 0.1197 * p_{water} + 3.018 * {p_{water}}^{0.5} + 0.5466 * p_{air} - 4.756 * {p_{air}}^{0.5}) \qquad (1)$$

4.3.3 PSD Calibration

The measured PSDs from the conditions listed in Table 2 are shown in Figure 11, Figure 12, Figure 13 and Figure 14 below. The left plot shows a direct comparison between the measured cumulative volume and the cumulative volume of the Appendix O requirement. On the right, a q-q plot is shown, indicating the percentual deviation of the cumulative volume. Furthermore, a linear regression has been performed, the R² values are displayed in the legend. Overall, the measured PSDs were within ±10% to ±15% compared to the Appendix O distributions. R² values of 0.949 to 0.991 indicate that the distributions are still very close to the requirements.

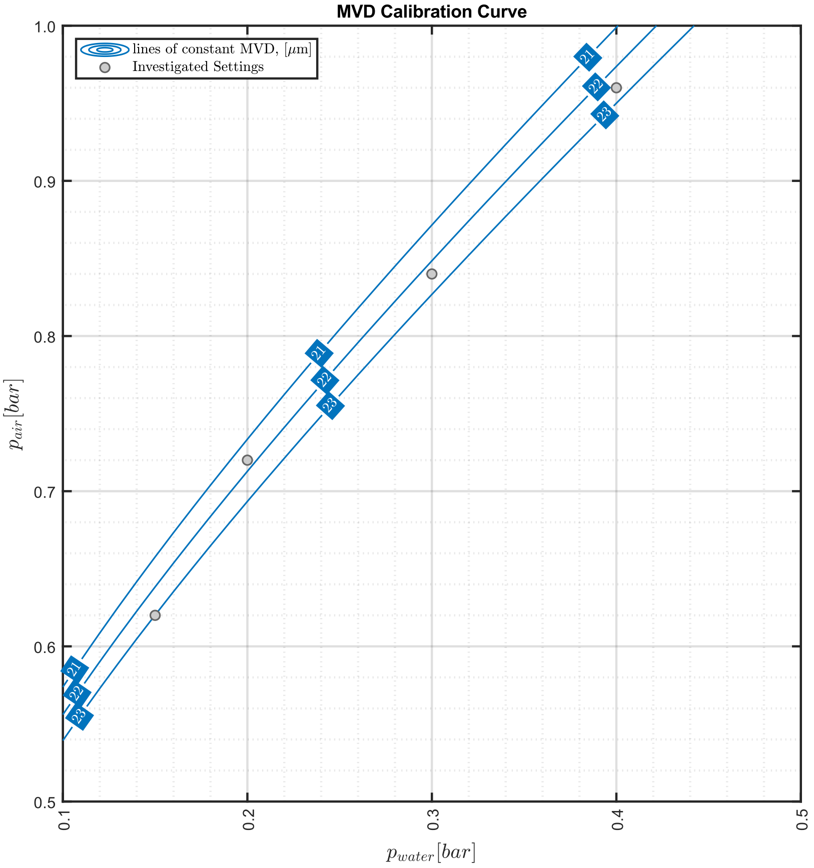

Figure 9: MVD calibration curve for FZDZ MVD < 40 μm conditions

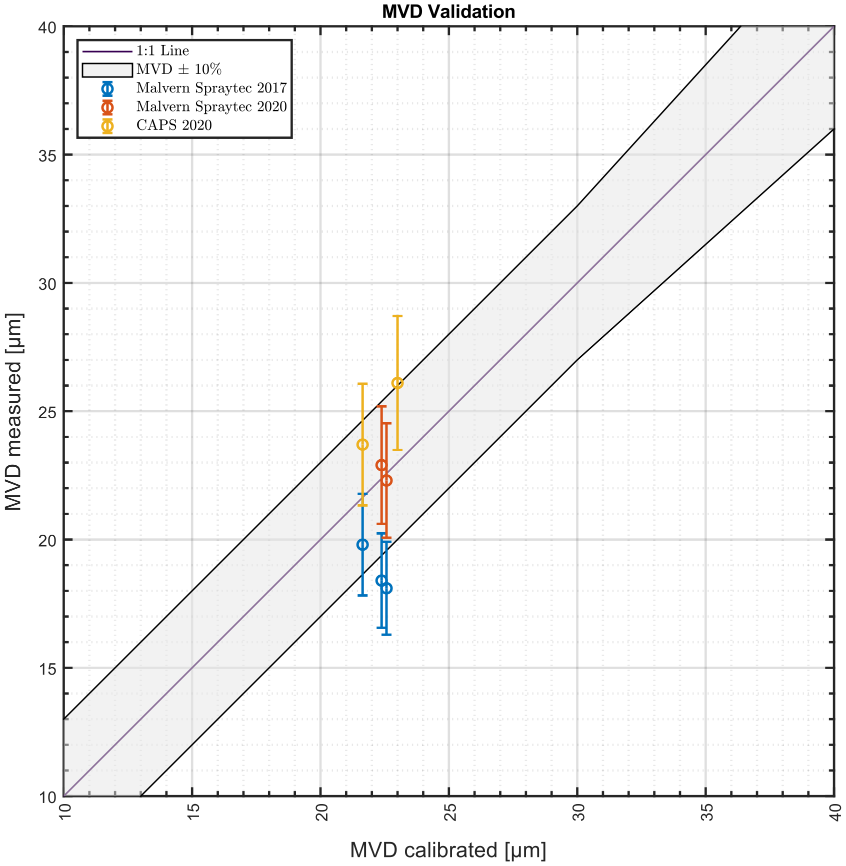

Figure 10: Comparison of calibrated and measured MVDs for all four FZDZ settings, below 30 μm the indicated limit is showing ±3 μm instead of ±10%

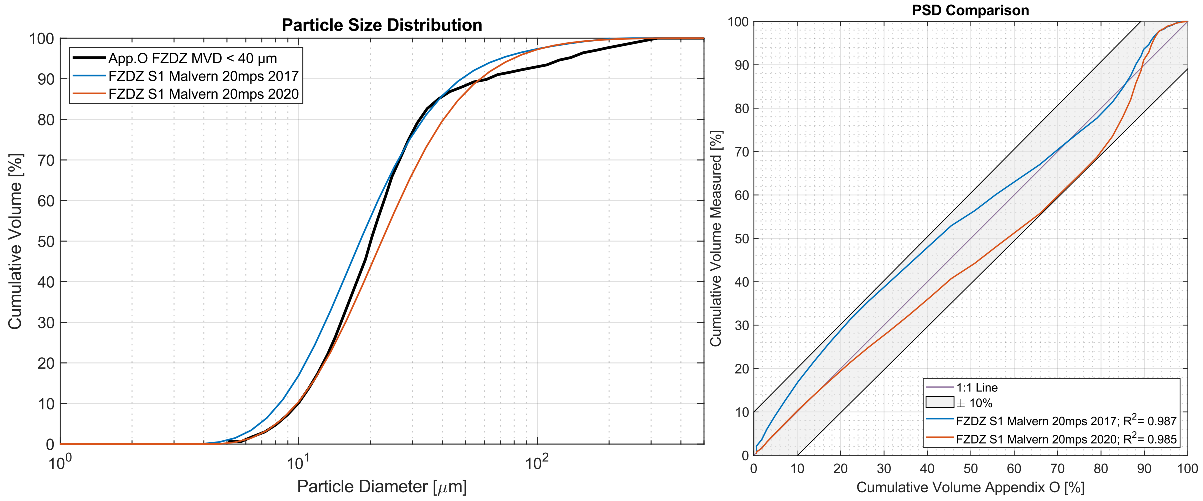

Figure 11: Measured PSDs for FZDZ S1 compared to Appendix O requirements, cumulative volume (left), q - q plot (right)

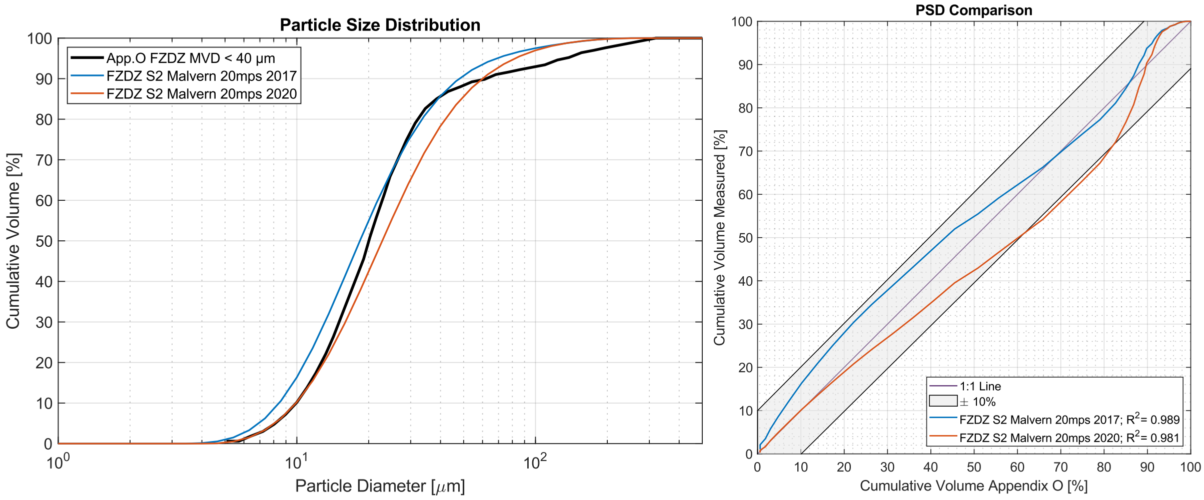

Figure 12: Measured PSDs for FZDZ S2 compared to Appendix O requirements, cumulative volume (left), q - q plot (right)

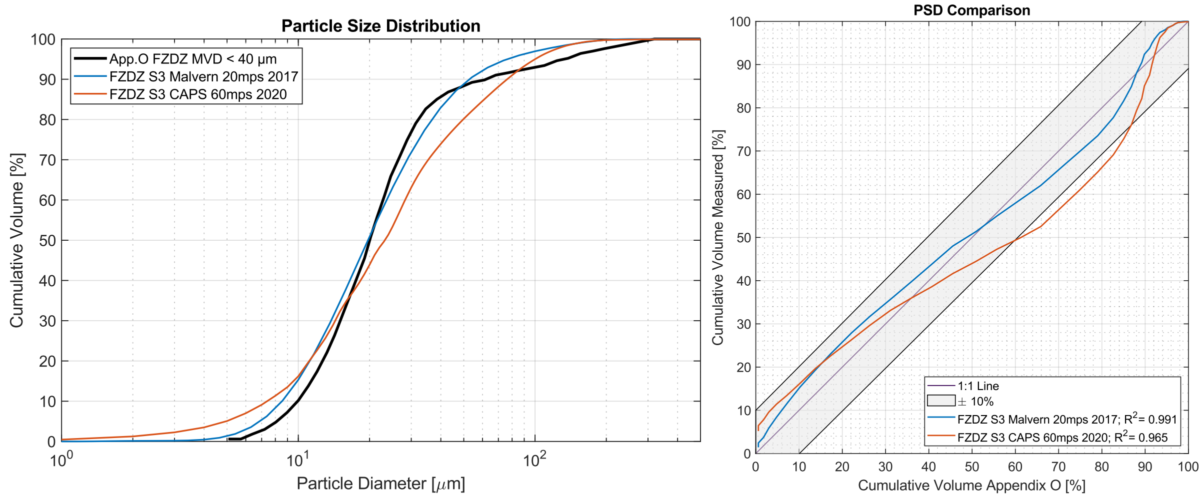

Figure 13: Measured PSDs for FZDZ S3 compared to Appendix O requirements, cumulative volume (left), q - q plot (right)

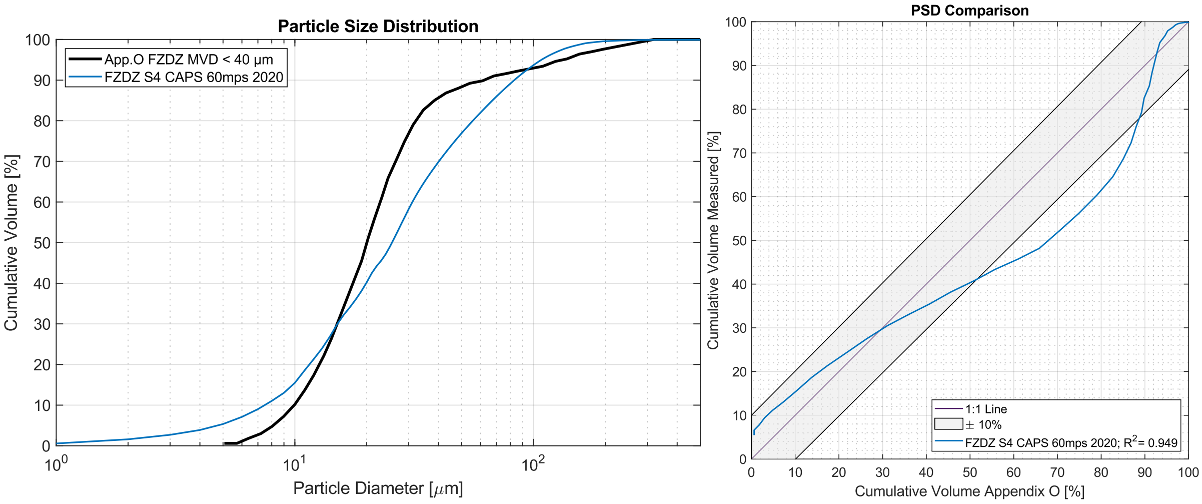

Figure 14: Measured PSDs for FZDZ S4 compared to Appendix O requirements, cumulative volume (left), q - q plot (right)

A separate calibration curve was generated to be able to also estimate the PSD for different spray nozzle settings. This curve describes the average PSD of all measurements from Table 2 and can be scaled with the calibrated MVD from Section 4.3.1. Table 3 lists the distribution, the diameters are calculated using Equation 2. The calibration curve should be capable of predicting the cumulative volume with an accuracy of ±10% (Figure 16).

$$diameter = MVD_{cal} * D_{Bin} \quad (2)$$

Table 3: PSD calibration, relative Bin size, volume percentage and cumulative volume

D_Bin	0.05	0.1	0.2	0.3	0.4	0.5	1.0	2.0	3.0	4.0	5.0	10.0	15.0	20.0	25.0
Vol [%]	0.05	0.85	1.0	3.0	5.0	5.0	32.0	32.0	10.0	5.0	2.0	4.0	0.1	0.0.	0.0
Cum. Vol. [%]	0.05	0.90	1.90	4.9	9.9	14.9	46.9	78.9	88.9	93.9	95.9	99.9	100	100	100

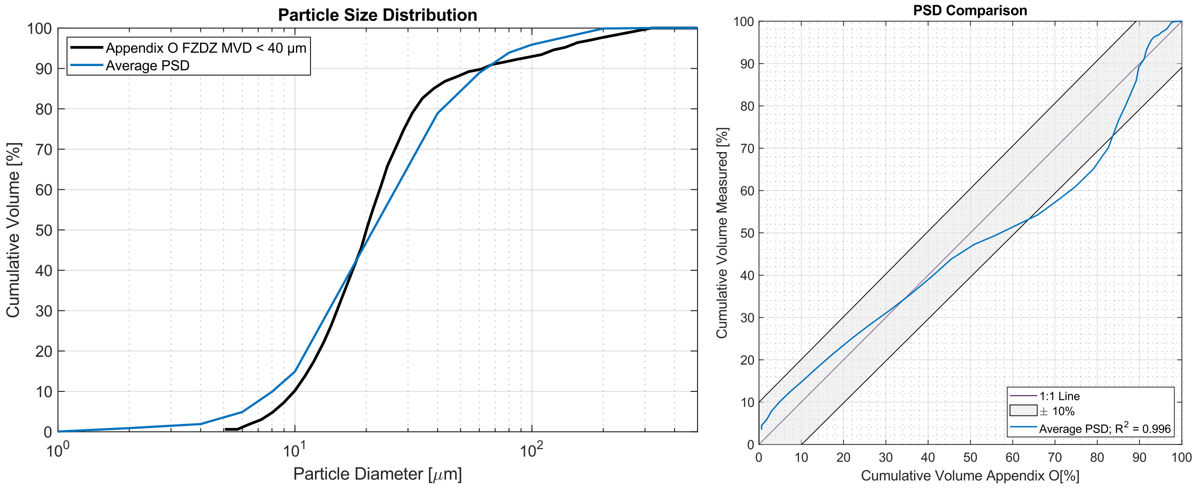

Figure 15: Average PSDs for FZDZ MVD < 40 µm compared to Appendix O requirements, cumulative volume (left), q - q plot (right)

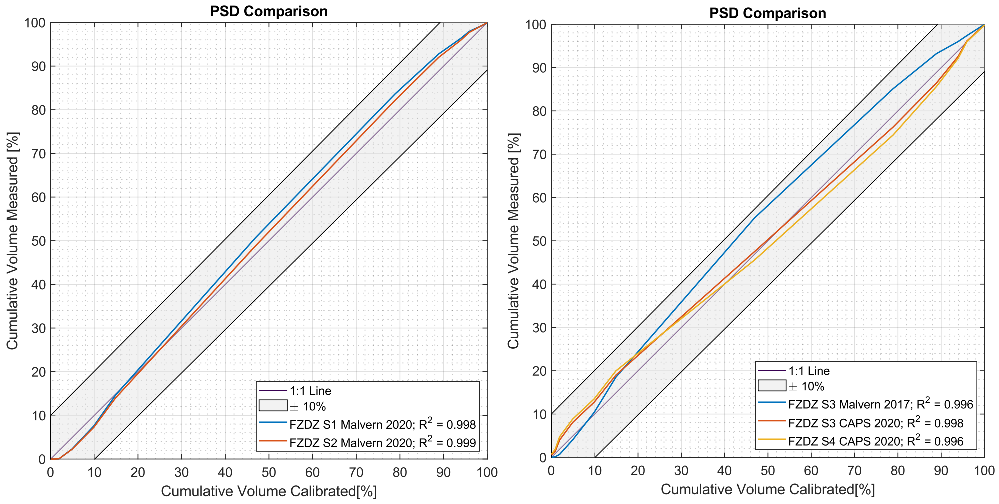

Figure 16: Comparison of measured cumulative volume versus prediction using the PSD calibration scaled with the MVD from the MVD calibration, FZDZ S1 & FZDZ S2 (left), FZDZ S3 & FZDZ S4 (right)

4.3.4 LWC Measurements

For the FZDZ MVD < 40 µm only very few measurement data are available. Table 4 lists the investigated conditions. The “lwc” column gives the airspeed independent water content, which is calculated according to Equation 3, where the number of operative circuits can be either 1 (only every second nozzle active) or 2 (all nozzles active). The test section LWC can be reduced by only operating half of the spray nozzles, which is possible due to the monomodal distribution.

$$lwc\ \left[\frac{g}{m^2 s}\right] = \frac{LWC\ \left[\frac{g}{m^3}\right] * TAS\ \left[\frac{m}{s}\right]}{operative\ circuits\ [-]} \qquad (3)$$

Table 4: LWC Measurements for FZDZ MVD < 40 µm conditions

Setting	p_{water}	p_{air}	Instrument	TAS [m/s]	SAT [°C]	lwc [g/m² s]	Year
FZDZ Sx	0.36	0.91	Blade	36	-18	6.22	2020
FZDZ Sx	0.29	0.83	Blade	36	-18	5.52	2020
FZDZ Sx	0.26	0.79	Blade	36	-18	5.33	2020
FZDZ Sx	0.24	0.76	Blade	36	-18	5.26	2020
FZDZ S3	0.20	0.72	Blade	36	-18	4.75	2020
FZDZ S3	0.20	0.72	Waterflow	60	2	5.40	2020
FZDZ S4	0.15	0.62	Waterflow	60	2	4.80	2020
FZDZ S3	0.20	0.72	CAPS	60	2	5.75	2020
FZDZ S4	0.15	0.62	CAPS	60	2	4.87	2020

4.3.5 LWC Calibration

Similar to the MVD, the spray nozzle pressure range is also within the standard LWC calibration for the atomizing nozzles. Therefore, the standard LWC calibration is used to calculate the LWC for these conditions (Equation 4). Figure 17 shows the calibration curve, the investigated settings are marked. The blue lines give the upper and lower air pressure limits for the corresponding water pressures. Figure 18 shows a comparison of the calibrated and measured water contents of the conditions listed in Table 4. The measurements were within 20% of the calibrated values, a linear fit of the measurement data gives a slope of 0.9449 indicating, that the standard calibration curve is able to predict the LWC with good enough accuracy.

$$lwc_s = \exp\big(15.71 - 3.586 * p_{water} + 6.776 * {p_{water}}^{0.5} .* log(p_{water}) - 8.681 * {p_{water}}^{0.5} + 3.253 * log(p_{water}) + 0.4407 * p_{air} * log(p_{air}) - 2.087 * {p_{air}}^{0.5} * log(p_{air})\big) \quad (4)$$

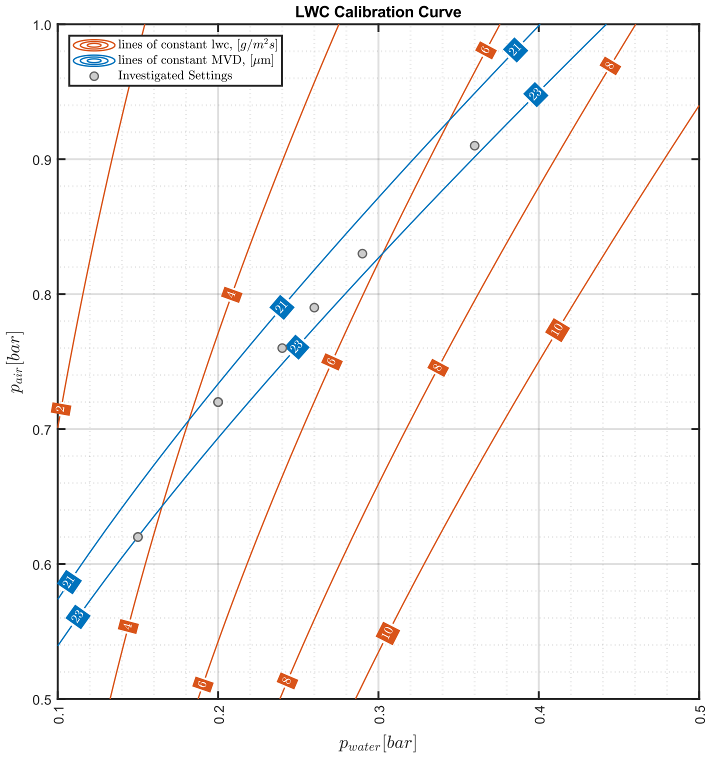

Figure 17: LWC calibration curve for FZDZ MVD < 40 µm conditions

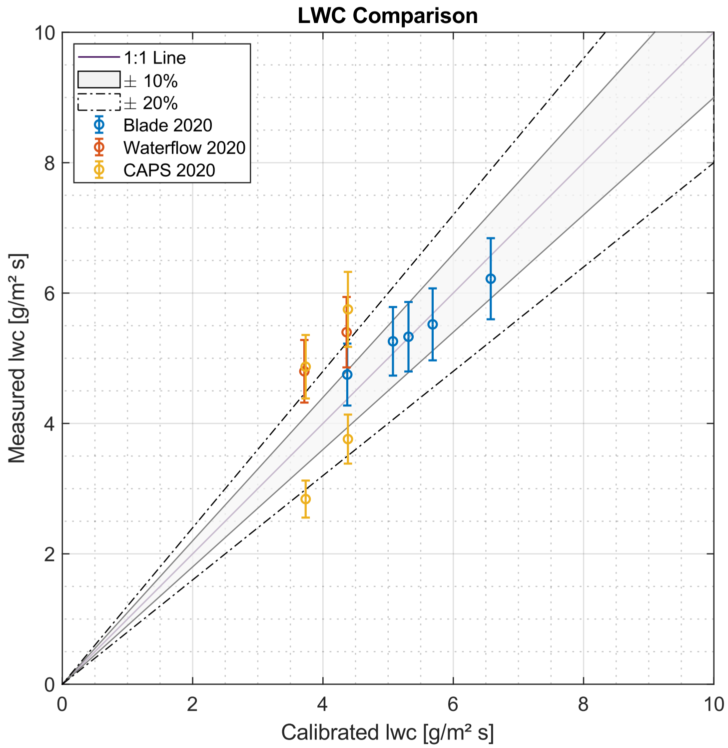

,

Figure 18: Comparison of calibrated and measured liquid water contents for FZDZ MVD < 40 µm

The achievable LWC envelope for different test section airspeeds is shown in Figure 19. The lowest possible LWC at 80 m/s is 0.05 g/m³, the highest is 0.18 g/m³. At 40 m/s the lower limit is 0.10 g/m³ and the upper limit is 0.35 g/m³.

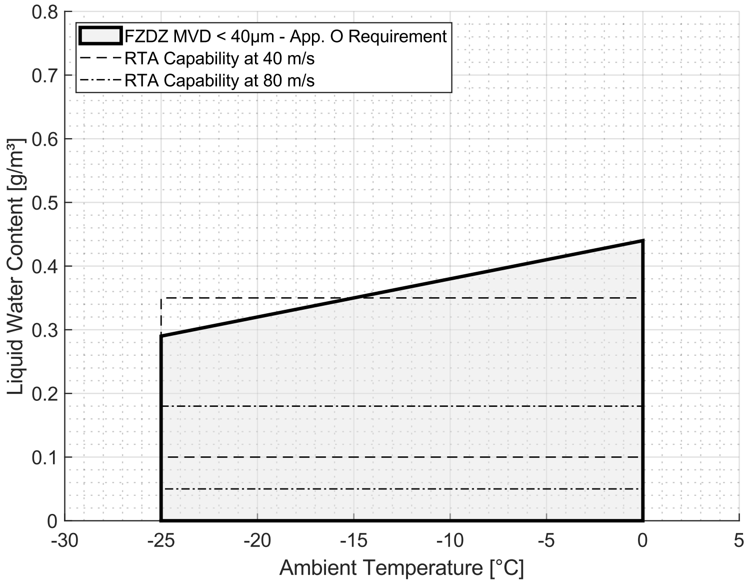

Figure 19: RTA LWC envelope compared to Appendix O requirement for FZDZ with an MVD of less than 40 µm, for 40 m/s and 80 m/s

4.3.6 LWC Uniformity

Figure 20 shows the result of a typical ice accretion grid measurement for a 20 µm Appendix C condition. No specific grid measurements of the settings listed in Table 1 or Table 4 have been performed. In Figure 21 the resulting uniformity plot from a test section mapping using the Nevzorov Probe I shown. The “FZDZ S3” spray nozzle setting was investigated at an airspeed of 40 m/s.

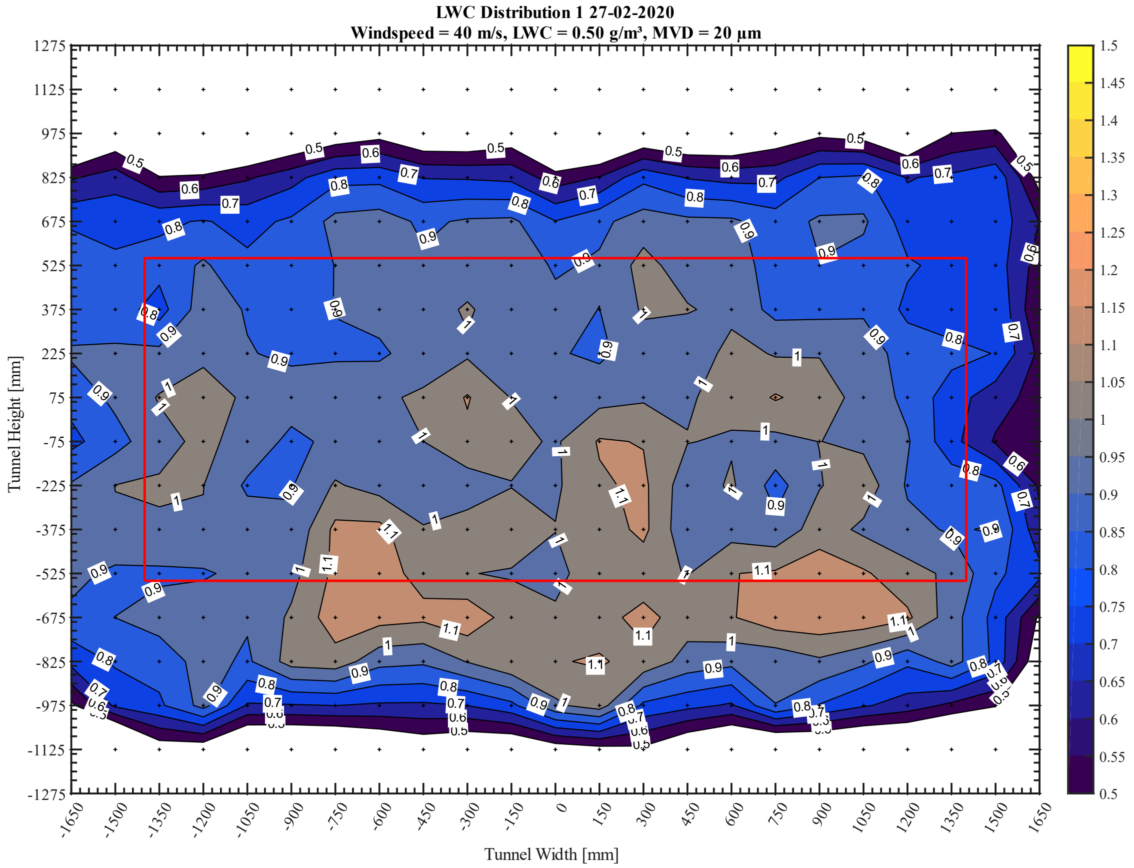

Figure 20: Ice accretion grid measurement of LWC Uniformity, the red frame marks the area of interest for wing tests

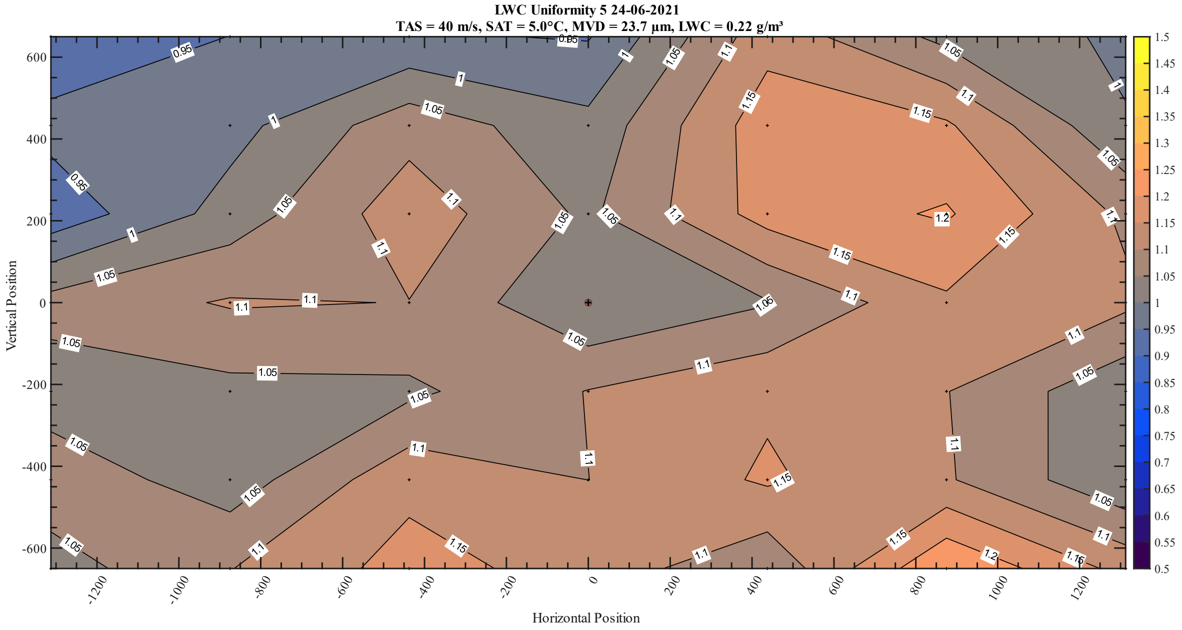

Figure 21: LWC Uniformity measured with Nevzorov probe on traversing system, spray bars 3-11 were active

4.4 Freezing Drizzle MVD > 40 µm

For Freezing Drizzle (FZDZ) with a Median Volume Diameter (MVD) of larger than 40 µm, MVD, Particle size distribution (PSD) and Liquid Water Content (LWC) investigations have been performed during internal, nationally funded (“FFG Aviation Icing Tests II-IV” and “FFG AquaSense”) and internationally funded (“ICE GENESIS”) research projects. The Requirements on the PSD and the LWC range is shown in Figure 22.

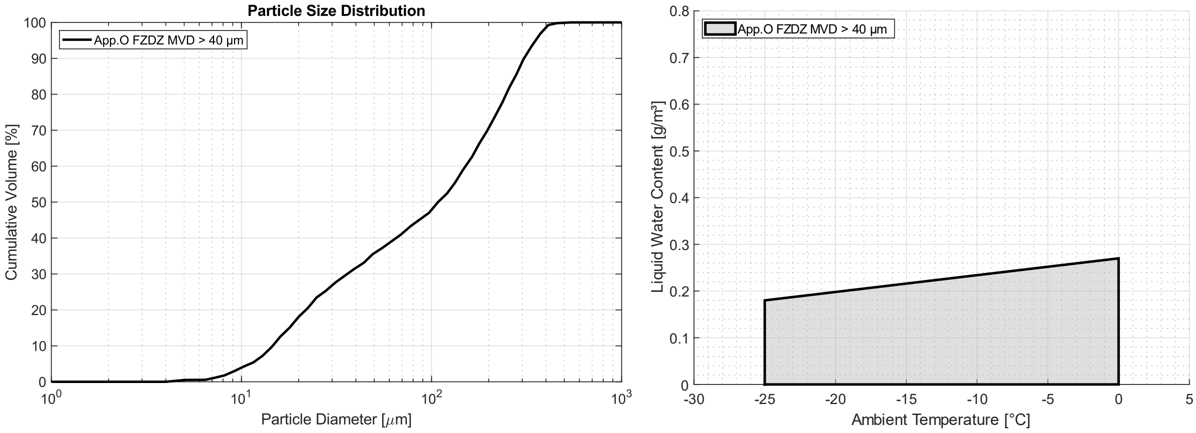

Figure 22: Appendix O Freezing Drizzle MVD > 40 µm PSD (left) and LWC range (right)

According to Cober and Isaac [1, p. 271] the MVD of FZDZ MVD > 40 µm conditions should be in the range of 110 µm with a maximum diameter of 474 µm. Figure 23 shows the individual measured PSDs and the average cumulative mass spectrum [2]. The 99.0% LWC of all cloud measurements was 0.27 g/m³, which is used as the upper limit in Appendix O, the maximum observed LWC was 0.39 g/m³ [1, pp. 278-280].

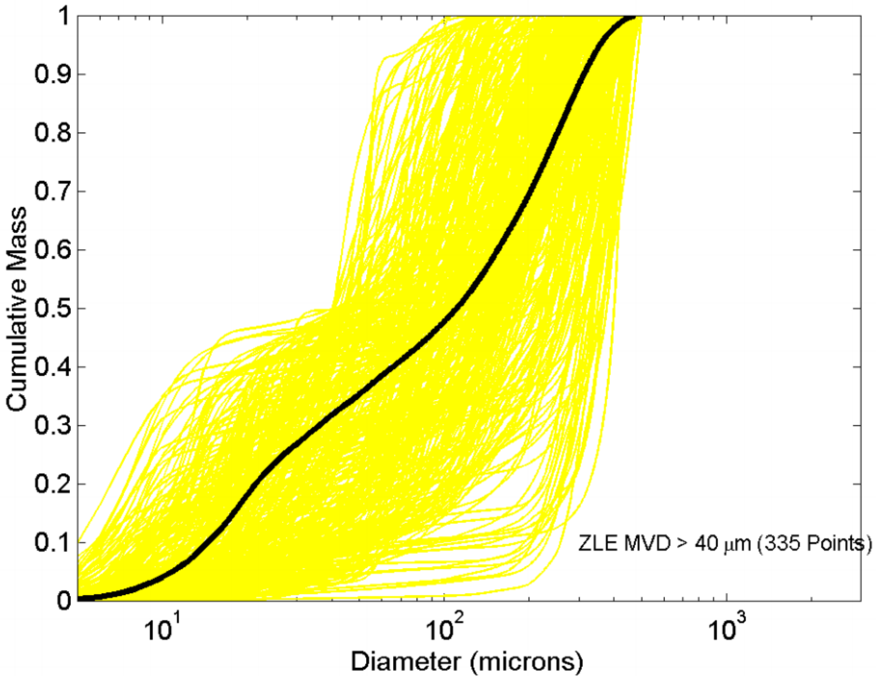

Figure 23: Average Cumulative Mass Spectrum for FZDZ MVD > 40 µm compared to each individual cumulative mass spectra [2, p.44]

Table 5 lists the four settings which have been investigated in the RTA IWT. Each of the eleven spray bars of the RTA spray bar system has two individually controllable circuits. This is used to create the required bimodal distribution for FZDZ MVD > 40 µm. Both circuits use the standard atomizing nozzles, which are also used for the generation of Appendix C conditions. In order to improve the cloud uniformity, the spray nozzles for the large and small mode are arranged in an alternating pattern.

Table 5: Investigated Spray bar settings for FZDZ MVD > 40 µm conditions

Setting	p_{water} 1 [bar]	p_{air} 1 [bar]	p_{water} 2 [bar]	p_{air} 2 [bar]
FZDZ L1	0.35	0.80	0.20	0.20
FZDZ L2	0.25	0.72	0.15	0.15
FZDZ L3	0.50	1.30	0.20	0.20
FZDZ L4	0.50	1.30	0.15	0.15

4.4.1 MVD / PSD Measurements

The MVDs and PSDs of the settings mentioned in Table 5 were measured using the Malvern Spraytec instrumentation with the 300 mm lens assembly and / or the CAPS or the FCDP/2D-S probe from Droplet Measurement Technologies. Table 6 lists the resulting MVDs. The detailed PSDs are shown in Section 4.4.3.

Table 6: MVD / PSD Measurements for FZDZ MVD > 40 µm conditions

Setting	Instrument	TAS [m/s]	SAT [°C]	MVD [µm]	Year
FZDZ L1	Malvern Spraytec	20	2	92.0	2017
FZDZ L2	Malvern Spraytec	20	2	100.5	2017
FZDZ L3	Malvern Spraytec	40	2	93.5	2019
FZDZ L4	Malvern Spraytec	40	2	109.3	2019
FZDZ L1	FCDP/2D-S	60	2	91.7	2019
FZDZ L2	FCDP/2D-S	60	2	92.9	2019
FZDZ L1	CAPS	60	2	84.3	2020
FZDZ L2	CAPS	60	2	94.2	2020
FZFZ L3	CAPS	60	2	83.4	2020
FZDZ L4	CAPS	60	2	90.0	2020

4.4.2 MVD Calibration

Due to the bimodal nature of the FZDZ distribution, the MVD is calibrated based on a combination of the small and the large mode. For the small Mode the standard Appendix C calibration curve is used. For the large mode, a separate calibration curve (Equation 5) was created by fitting measurement data from different instruments (Malvern, FCDP/2D-S and CAPS).

$$MVD_l = 172.3 - 47.66 * p_{water} - 264.6 * p_{air} \quad (5)$$

To derive the combined MVD of both modes, the LWC ratio calculated by the LWC calibration curves (see Section 4.4.5) is used as shown in Equation 6.

$$MVD = MVD_s * \frac{lwc_s}{lwc_s + lwc_l} + MVD_l * \left(1 - \frac{lwc_s}{lwc_s + lwc_l}\right) \quad (6)$$

Figure 24 and Figure 25 show the resulting calibration curves for the small and large mode respectively. Figure 26 shows the calculated MVDs for the settings listed in Table 6 compared to the measured ones, indicating a very good agreement in the range of ±10%.

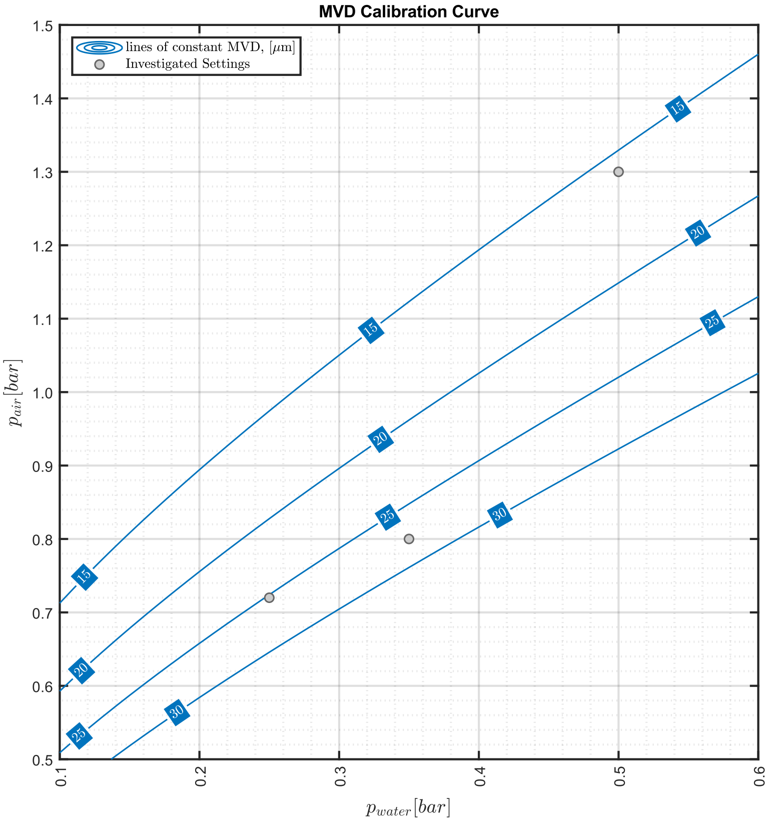

Figure 24: MVD calibration curve for small Mode of FZDZ MVD > 40 µm conditions

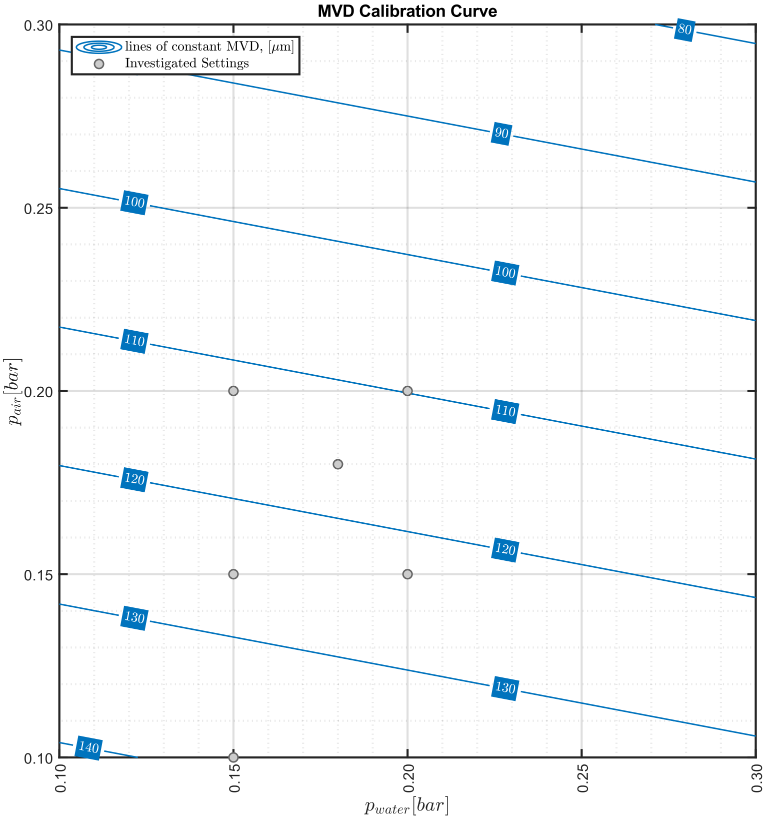

Figure 25: MVD calibration curve for large Mode of FZDZ MVD > 40 µm conditions

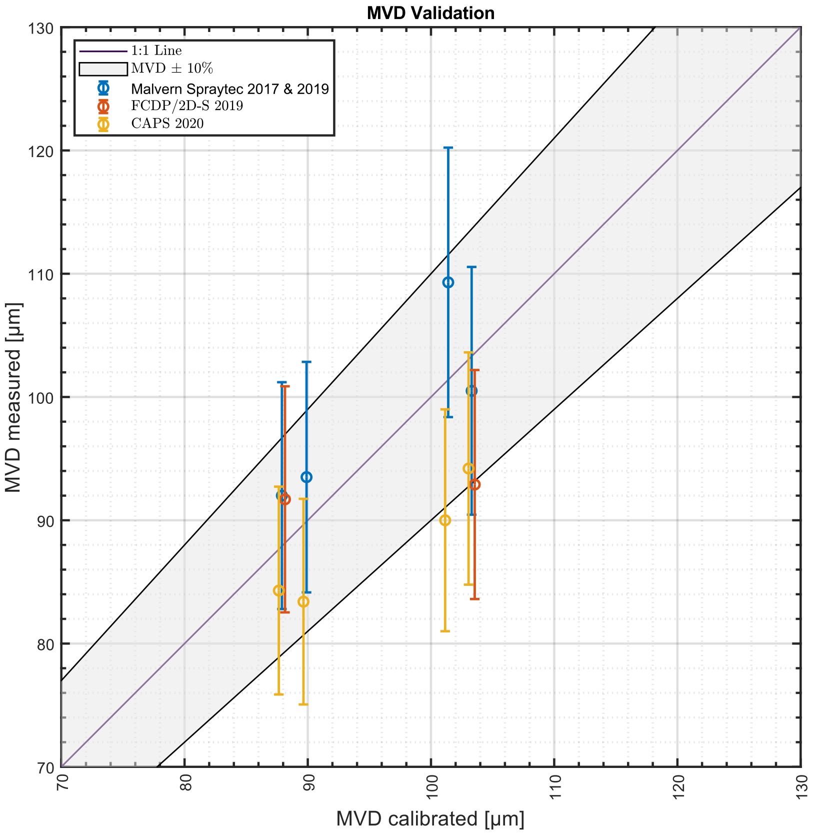

Figure 26: Comparison of calibrated and measured MVDs for all investigated FZDZ MVD > 40 µm settings

4.4.3 PSD Calibration

In addition to the MVD calibration, also a PSD calibration was derived, in order to predict the average PSD for different FZDZ MVD > 40 µm settings. Figure 27 to Figure 30 show the measured distributions (left), on the right, q-q plots are shown, indicating the percentual deviation of the cumulative volume compared to the Appendix O requirement. Furthermore, a linear regression has been performed, the R^2 values are displayed in the legend. Overall, the measured PSDs were within ±10% to ±20% compared to the Appendix O distributions. R^2 values of 0.955 to 0.997 indicate that the distributions are still very close to the requirements.

The PSD calibration is based on Langmuir distributions (“E” for small mode and “F” for large mode), which are generated with the MVDs of the corresponding MVD calibrations for the small and the large mode (see Section 4.4.2) and corrected with a scaling factor in order to better match the combined calibrated MVDs. The two distributions are then fitted with a gaussian bell curve. The cumulative volume is then recreated from the two distributions by using the ratio between the calibrated LWCs of the small and the large mode (see Section 4.4.5).

Figure 31 shows the resulting cumulative volumes of the calibrated PSDs (left) and a comparison with the Appendix O requirement for FZDZ MVD > 40 µm (right). The calibrated PSDs match the requirement within ±15%, where FZDZ L4 showed the most promising result with deviations of less than ±10%. In Figure 32, the calibrated and measured cumulative volumes are compared by means of a q-q plot. A good agreement between the calibration and the measurement was achieved, indicating deviation of less than ±10%.

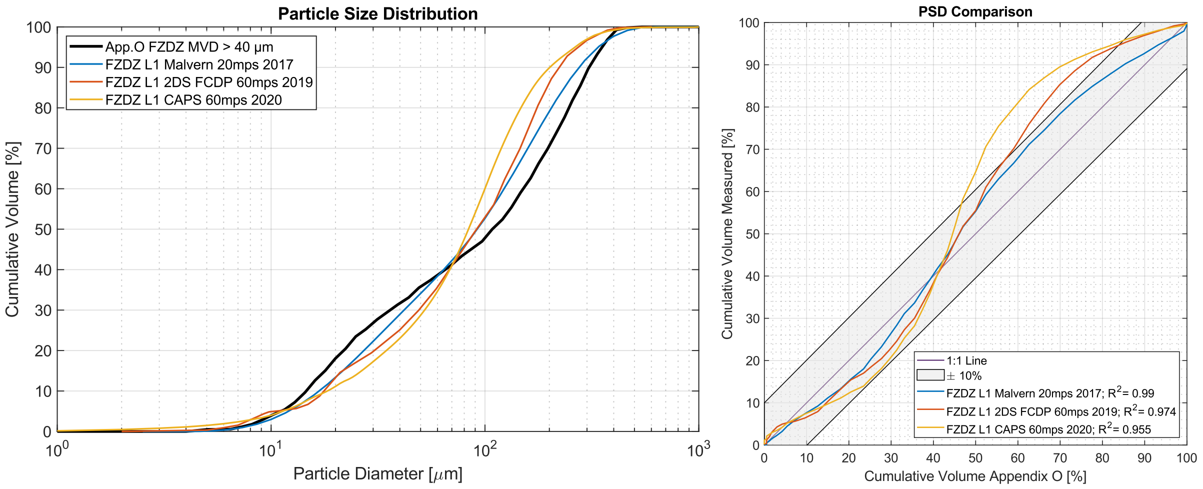

Figure 27: Measured PSDs for FZDZ L1 compared to Appendix O requirements, cumulative volume (left), q - q plot (right)

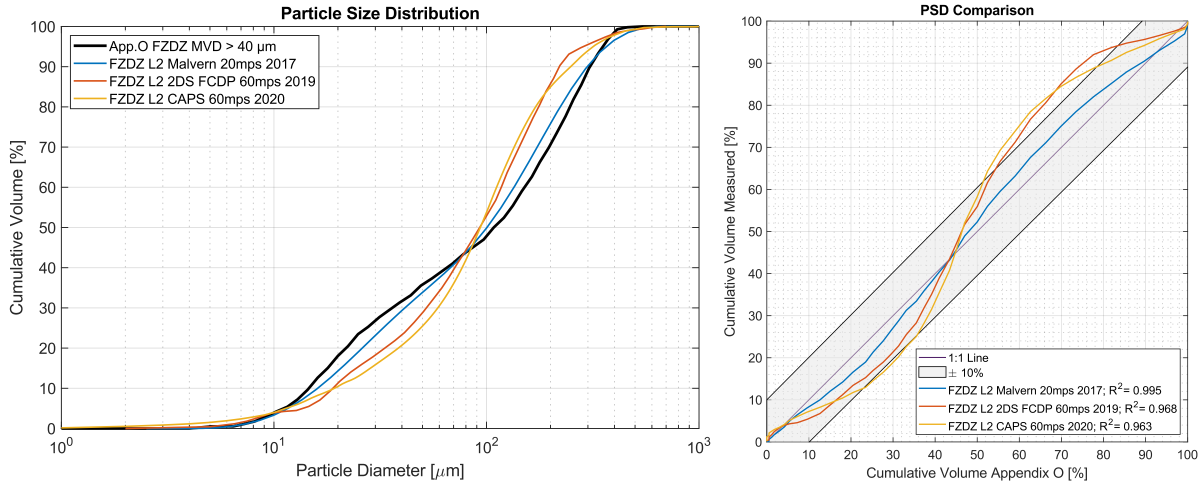

Figure 28: Measured PSDs for FZDZ L2 compared to Appendix O requirements, cumulative volume (left), q - q plot (right)

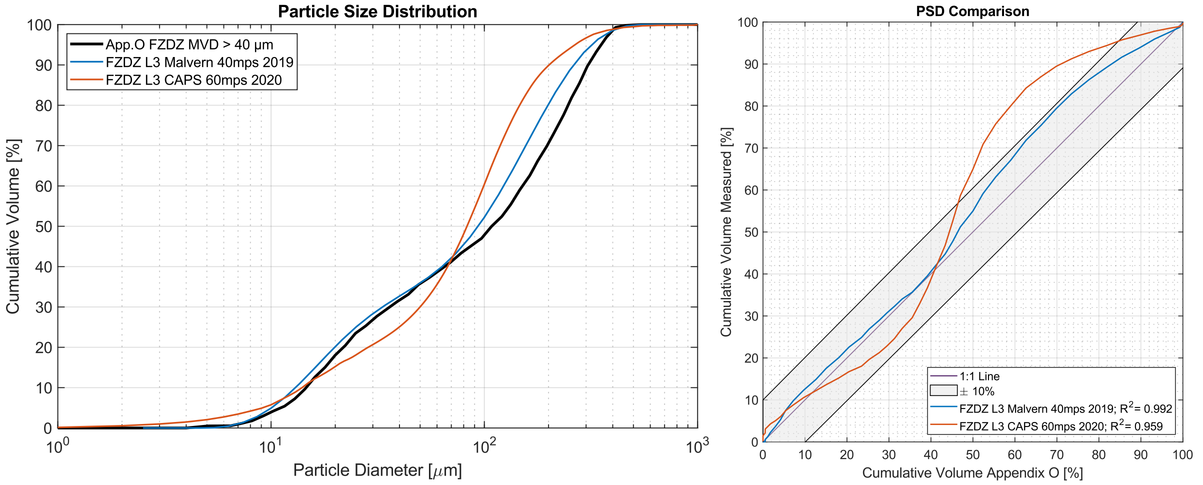

Figure 29: Measured PSDs for FZDZ L3 compared to Appendix O requirements, cumulative volume (left), q - q plot (right)

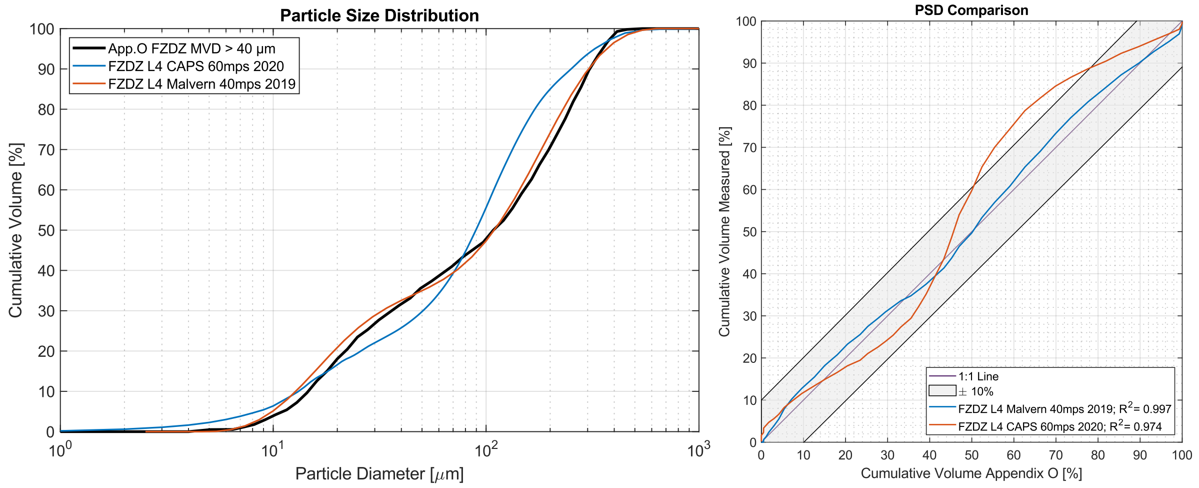

Figure 30: Measured PSDs for FZDZ L4 compared to Appendix O requirements, cumulative volume (left), q - q plot (right)

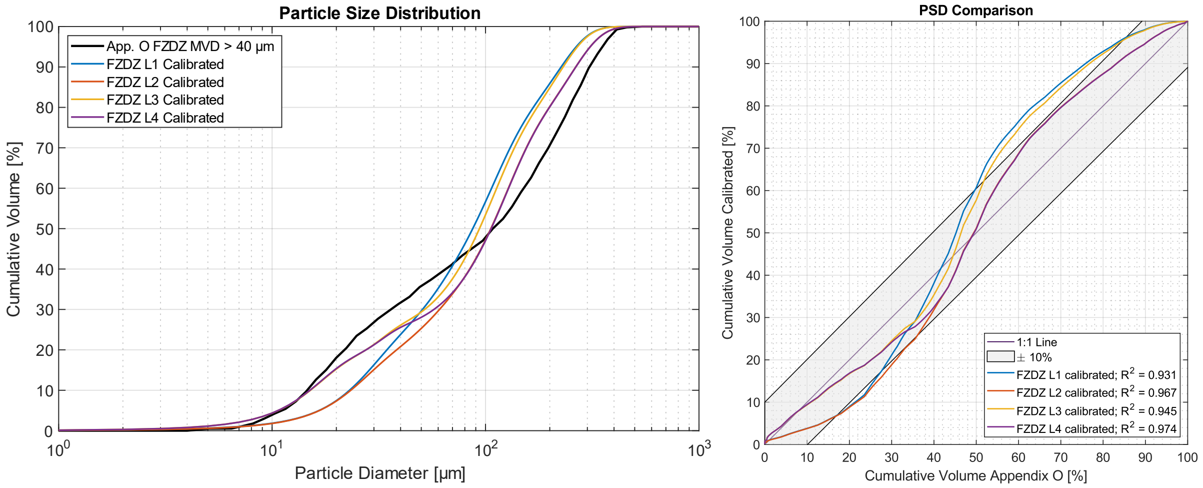

Figure 31: Calibrated PSDs of FZDZ MVD > 40 µm versus appendix O requirement, cumulative volume (left), q - q plot (right)

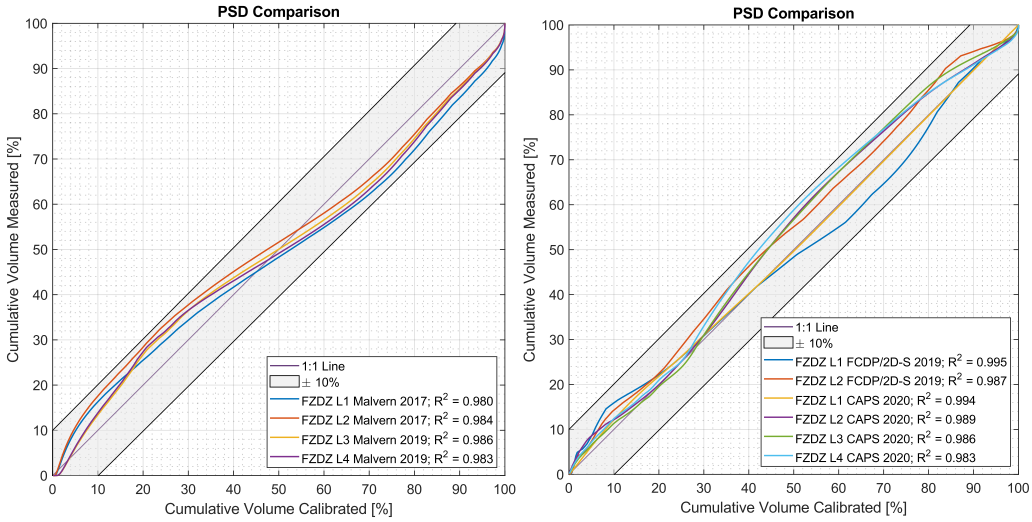

Figure 32: Comparison of measured cumulative volume versus prediction using the PSD calibration; Malvern measurements (left), FCDP/2D-S and CAPS measurements (right)

4.4.4 LWC Measurements

For the FZDZ MVD > 40 µm condition, LWC measurements from different instrumentation mainly for Setting 1 and 2 are available. Table 7 lists the investigated conditions. The "lwc" column gives the airspeed independent water content, which is calculated according to Equation 2, where the number of operative circuits has to be set to 1, as the bimodal distribution always requires both modes.

Table 7: LWC Measurements for FZDZ MVD > 40 µm conditions

Setting	Mode	Instrument	TAS [m/s]	SAT [°C]	LWC x V [g/m² s]	LWC [g/m³]	Year
FZDZ L1	Both	Blade	50	-18	31.50	0,63	2016
FZDZ L1	Both	Blade	55	-18	31.43	0,57	2016
FZDZ L1	Both	Blade	60	-18	31.43	0,52	2016
FZDZ L1	Both	Blade	65	-18	30.53	0,47	2016
FZDZ L1	Both	Blade	80	-18	31.43	0,39	2016
FZDZ L1	Both	WCM2000	50	-18	28.00	0,56	2016
FZDZ L1	Both	WCM2000	50	-5	27.50	0,55	2016
FZDZ L1	Both	WCM2000	50	-5	26.50	0,53	2016
FZDZ L1	Both	WCM2000	55	-5	23.66	0,43	2016
FZDZ L1	Both	WCM2000	60	-5	24.00	0,40	2016
FZDZ L1	Both	WCM2000	60	-5	24.00	0,40	2016
FZDZ L1	Both	WCM2000	70	-5	25.90	0,37	2016
FZDZ L1	Both	WCM2000	75	-5	27.00	0,36	2016
FZDZ L1	Both	WCM2000	80	-5	26.40	0,33	2016
FZDZ L1	Both	WCM2000	60	-5	26.40	0,44	2018
FZDZ L1	Both	WCM2000	50	-14	29.00	0,58	2018
FZDZ L1	Both	WCM2000	60	-14	31.20	0,52	2018
FZDZ L1	Both	WCM2000	60	-5	31.80	0,53	2018
FZDZ L1	Both	WCM2000	60	-5	31.20	0,52	2018
FZDZ L1	Both	WCM2000	50	-5	29.50	0,59	2018
FZDZ L1	Both	IKP	60	-5	40.20	0,67	2018
FZDZ L1	Both	IKP	50	-5	37.00	0,74	2018
FZDZ L1	Both	Nevzorov 8mm	30	-5	27.90	0,93	2019
FZDZ L1	Both	Nevzorov 8mm	30	-5	28.20	0,94	2019
FZDZ L1	Both	Nevzorov 8mm	30	-5	28.20	0,94	2019
FZDZ L1	Both	Nevzorov 8mm	30	-5	28.80	0,96	2019

Setting	Mode	Instrument	TAS [m/s]	SAT [°C]	LWC x V [g/m² s]	LWC [g/m³]	Year
FZDZ L1	Both	Nevzorov 8mm	30	-5	30.60	1,02	2019
FZDZ L1	Both	Nevzorov 8mm	50	-5	36.50	0,73	2019
FZDZ L1	Both	Nevzorov 8mm	50	-5	29.00	0,58	2019
FZDZ L1	Both	Nevzorov 8mm	60	-5	29.40	0,49	2019
FZDZ L1	Both	Nevzorov 8mm	50	-5	27.00	0,54	2019
FZDZ L1	Both	Nevzorov 8mm	60	-5	27.00	0,45	2019
FZDZ L1	Both	Nevzorov 8mm	60	-5	25.20	0,42	2019
FZDZ L1	Both	Nevzorov 8mm	50	-5	23.00	0,46	2019
FZDZ L1	Both	Nevzorov 12mm	30	-5	24.60	0,82	2019
FZDZ L1	Both	Nevzorov 12mm	30	-5	24.30	0,81	2019
FZDZ L1	Both	Nevzorov 12mm	30	-5	24.60	0,82	2019
FZDZ L1	Both	Nevzorov 12mm	30	-5	25.50	0,85	2019
FZDZ L1	Both	Nevzorov 12mm	30	-5	27.00	0,90	2019
FZDZ L1	Both	Nevzorov 12mm	50	-5	30.00	0,60	2019
FZDZ L1	Both	Nevzorov 12mm	50	-5	21.00	0,42	2019
FZDZ L1	Both	Nevzorov 12mm	60	-5	27.00	0,45	2019
FZDZ L1	Both	Nevzorov 12mm	50	-5	24.50	0,49	2019
FZDZ L1	Both	Nevzorov 12mm	60	-5	21.60	0,36	2019
FZDZ L1	Both	Nevzorov 12mm	60	-5	22.20	0,37	2019
FZDZ L1	Both	Nevzorov 12mm	50	-5	21.00	0,42	2019
FZDZ L1	Both	Waterflow	60	2	28.80	0,48	2020

Setting	Mode	Instrument	TAS [m/s]	SAT [°C]	LWC x V [g/m² s]	LWC [g/m³]	Year
FZDZ L1	Both	CAPS	60	2	34.80	0,58	2020
FZDZ L2	Both	WCM2000	60	-5	22.20	0,37	2018
FZDZ L2	Both	WCM2000	50	-5	27.00	0,54	2018
FZDZ L2	Both	WCM2000	50	-14	28.00	0,56	2018
FZDZ L2	Both	WCM2000	60	-5	30.00	0,50	2018
FZDZ L2	Both	WCM2000	60	-5	30.60	0,51	2018
FZDZ L2	Both	WCM2000	50	-5	20.50	0,41	2018
FZDZ L2	Both	IKP	60	-5	33.60	0,56	2018
FZDZ L2	Both	IKP	50	-5	30.50	0,61	2018
FZDZ L2	Both	Nevzorov 8mm	30	-5	26.10	0,87	2019
FZDZ L2	Both	Nevzorov 8mm	30	-5	24.60	0,82	2019
FZDZ L2	Both	Nevzorov 8mm	50	-5	24.50	0,49	2019
FZDZ L2	Both	Nevzorov 8mm	50	-5	33.50	0,67	2019
FZDZ L2	Both	Nevzorov 8mm	60	-5	29.40	0,49	2019
FZDZ L2	Both	Nevzorov 8mm	60	-5	21.00	0,35	2019
FZDZ L2	Both	Nevzorov 8mm	60	-5	22.80	0,38	2019
FZDZ L2	Both	Nevzorov 8mm	50	-5	17.00	0,34	2019
FZDZ L2	Both	Nevzorov 12mm	30	-5	23.70	0,79	2019
FZDZ L2	Both	Nevzorov 12mm	30	-5	21.90	0,73	2019
FZDZ L2	Both	Nevzorov 12mm	50	-5	28.50	0,57	2019
FZDZ L2	Both	Nevzorov 12mm	50	-5	37.00	0,74	2019
FZDZ L2	Both	Nevzorov 12mm	60	-5	25.80	0,43	2019
FZDZ L2	Both	Nevzorov 12mm	60	-5	19.20	0,32	2019
FZDZ L2	Both	Nevzorov 12mm	60	-5	21.00	0,35	2019

Setting	Mode	Instrument	TAS [m/s]	SAT [°C]	LWC x V [g/m² s]	LWC [g/m³]	Year
FZDZ L2	Both	Nevzorov 12mm	50	-5	15.00	0,30	2019
FZDZ L2	Both	Waterflow	60	2	24.00	0,40	2020
FZDZ L2	Both	CAPS	60	2	27.00	0,45	2020
FZDZ L3	Both	Waterflow	60	2	27.00	0,45	2020
FZDZ L3	Both	CAPS	60	2	33.00	0,55	2020
FZDZ L4	Both	Waterflow	60	2	25.20	0,42	2020
FZDZ L4	Both	CAPS	60	2	28.20	0,47	2020

4.4.5 LWC Calibration

Similar to the MVD, the LWC calibration curve was also split into two parts, one for the small mode, which is equal to the standard LWC calibration and one for the large mode focusing on the low water- and air-pressure settings (Equation 7).

$$lwc_l = 43.33 + 125.4 * p_{water} - 408.7 * p_{air} - 1288 * p_{water}^2 + 2145 * p_{water} * p_{air} \quad (7)$$

Figure 33 shows the calibration curve for the small mode, the investigated settings are marked. The blue lines give the upper and lower air pressure limits for the corresponding water pressures. Figure 34 shows the calibration curve for the large mode, the investigated settings are marked as well. In order to calculate the total combined LWC, Equation 8 is used.

$$LWC\ [\frac{g}{m^3}] = \frac{lwc_s\ [\frac{g}{m^2 s}]\ +\ lwc_l\ [\frac{g}{m^2 s}]}{TAS\ [\frac{m}{s}]} \quad (8)$$

In Figure 35 a comparison between the calibrated and the measured liquid water contents is shown. Most measurements were within 15% of the calibrated values, with the IKP and CAPS measuring slightly higher LWCs (up to +25%) but those instruments also have the highest measurement uncertainty. A linear fit of the measurement data gives a slope of about 1.10, indicating a conservative approach, where the measured LWC is slightly higher compared to the calibration.

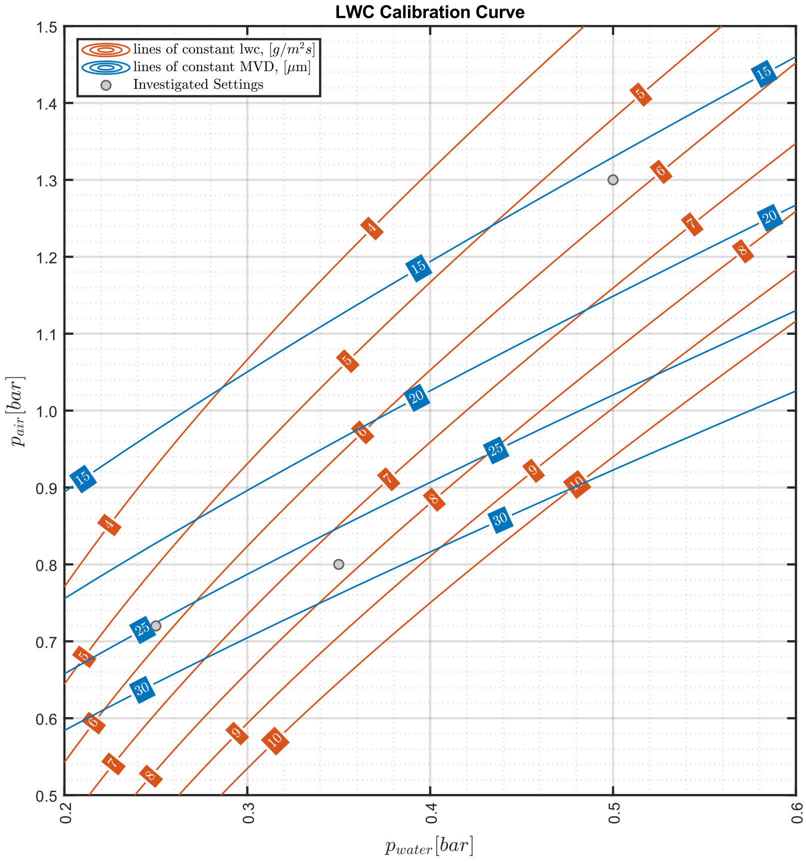

Figure 33: LWC calibration curve for small Mode of FZDZ MVD > 40 µm conditions

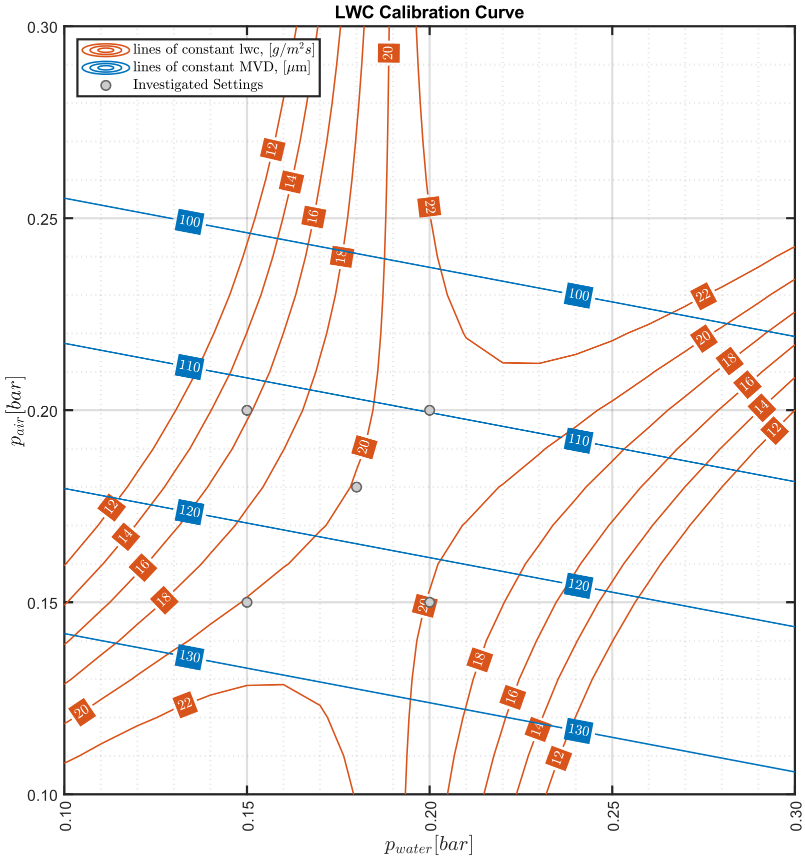

Figure 34: LWC calibration curve for large Mode of FZDZ MVD > 40 µm conditions

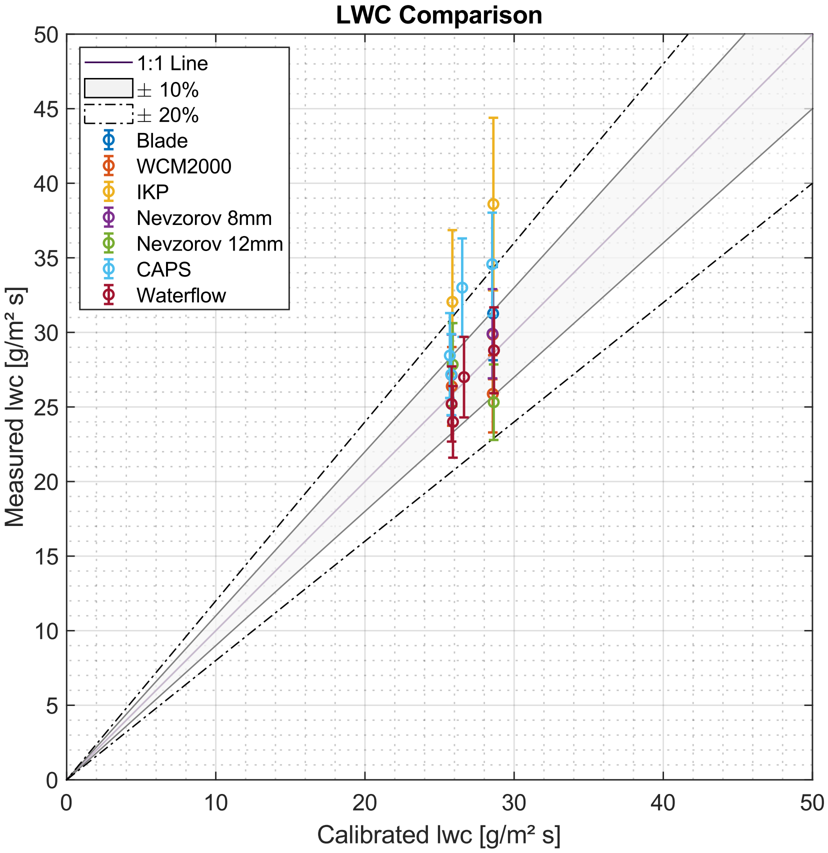

Figure 35: Comparison of calibrated and measured liquid water contents for FZDZ MVD > 40 µm

The achievable LWC envelope for different test section airspeeds is shown in Figure 36. The lowest possible LWC at 80 m/s is 0.32 g/m³, the highest is 0.35 g/m³. At 40 m/s the lower limit is 0.64 g/m³ and the upper limit is 0.71 g/m³.

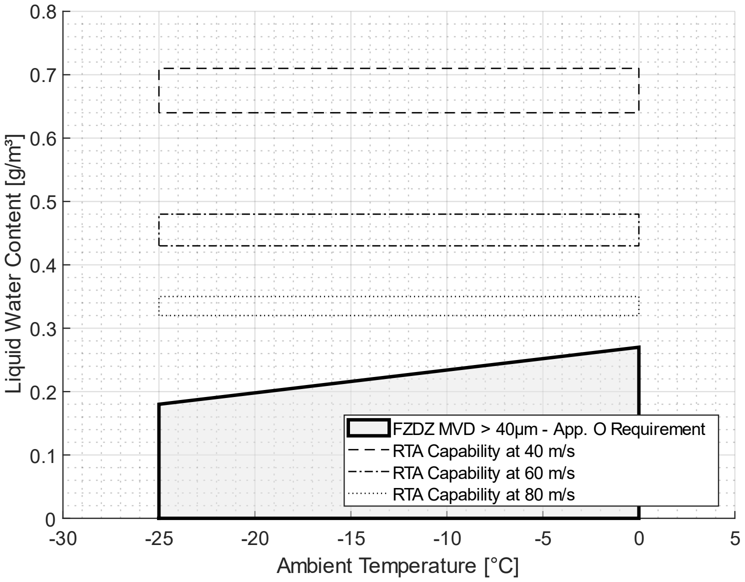

Figure 36: RTA LWC envelope compared to Appendix O requirement for FZDZ with an MVD of larger than 40 µm, for 40 m/s, 60 m/s and 80 m/s

4.4.6 LWC Uniformity

The LWC Uniformity has been investigated using a standard ice accretion grid and a Nevzorov Probe (from DLR) mounted on a traversing system (as shown in Figure 37). The Nevzorov mappings were performed at an air temperature of 5°C, as the traversing system cannot be operated under icing conditions.

The resulting uniformity plot from the accretion grid measurement is shown in Figure 38. The "FZDZ L1" spray nozzle setting was used. The measurement was performed at a test section airspeed of 60 m/s, at an ambient temperature of -18°C. Overall a very uniform distribution (±10%) was observed for the majority of the test section. In the lower region some peaks (up to 20% increased LWCs) were observed.

The Nevzorov Probe mappings were performed at an air temperature of 5°C, as the traversing system cannot be operated under icing conditions. In Figure 39 and Figure 40 the resulting uniformity plots of setting "FZDZ L4" are shown for a test section airspeed of 40 m/s. Figure 41 shows the uniformity plot for the same setting at an airspeed of 60 m/s. Figure 42shows the LWC distribution with only the large mode from setting "FZDZ L4" active, at an airspeed of 40 m/s.

All measurements have shown good distributions with deviations within ±20% compared to the geometrical test section centre. Both methods have delivered very similar results, with regions of higher LWC in the lower area of the test section.

Figure 37: Photograph of traversing system with mounted Nevzorov Probe

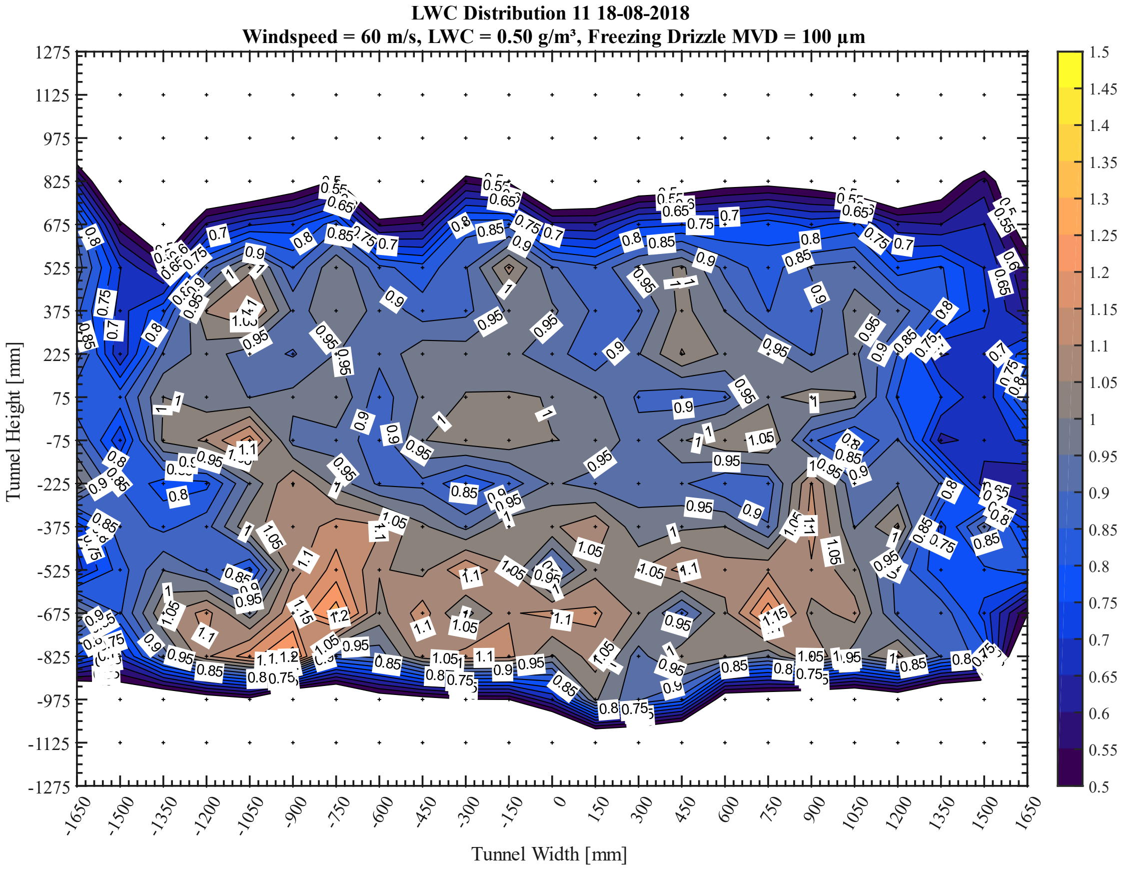

Figure 38: LWC Uniformity for "FZDZ L1" at a test section airspeed of 60 m/s, measured using the ice accretion grid

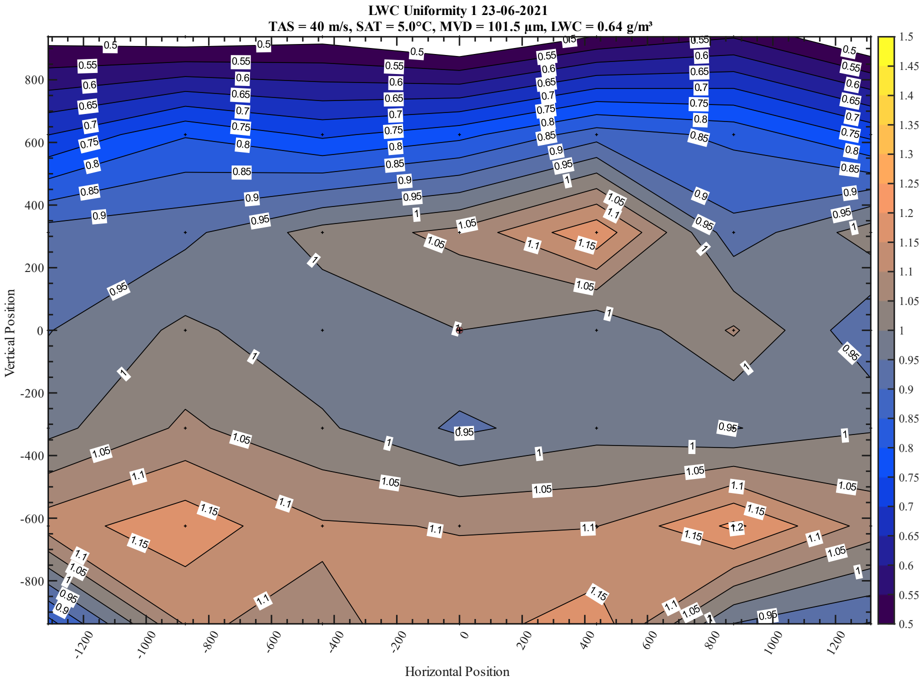

Figure 39: LWC Uniformity for "FZDZ L4" at a test section airspeed of 40 m/s, test section mapping with Nevzorov Probe, spray bars 3-10 were active

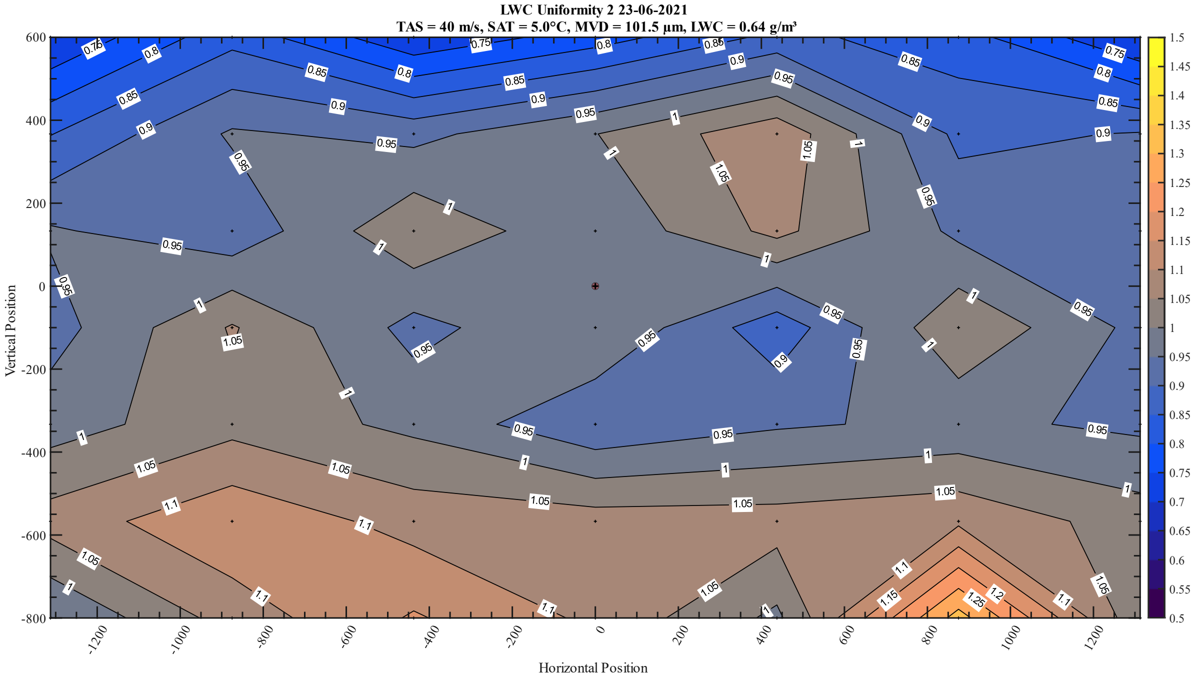

Figure 40: LWC Uniformity for "FZDZ L4" at a test section airspeed of 40 m/s, test section mapping with Nevzorov Probe, spray bars 3-11 were active

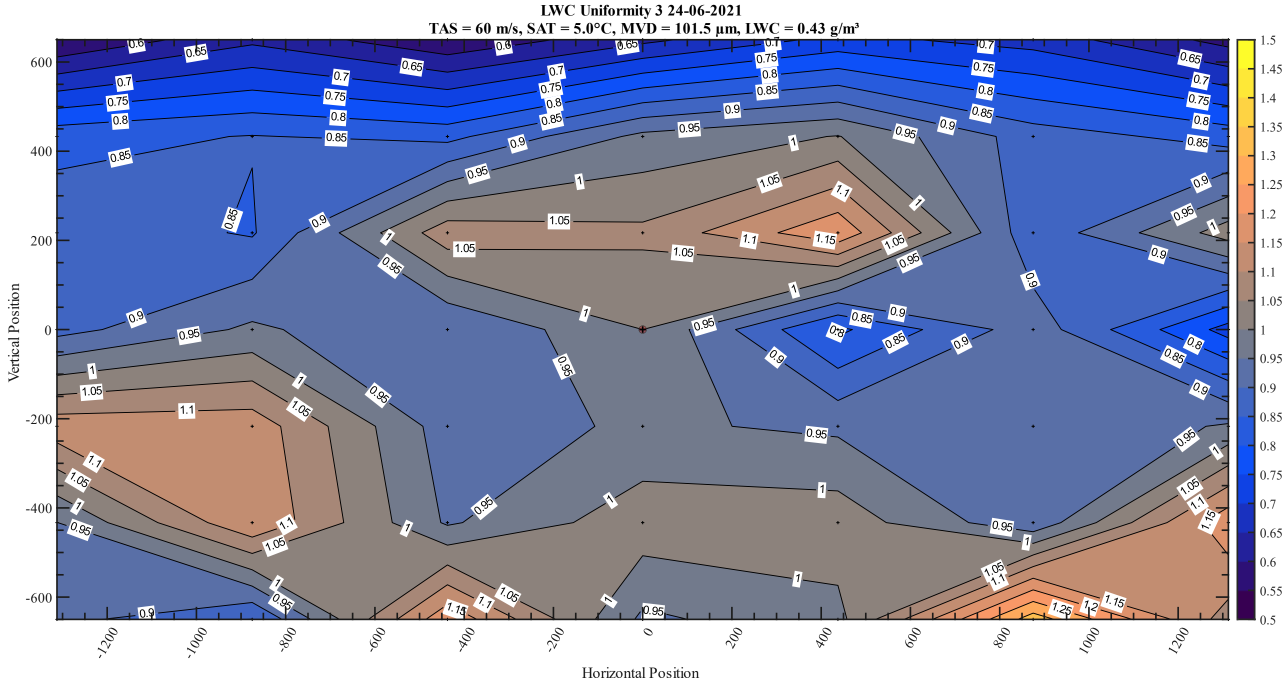

Figure 41: LWC Uniformity for "FZDZ L4" at a test section airspeed of 60 m/s, test section mapping with Nevzorov Probe, spray bars 3-11 were active

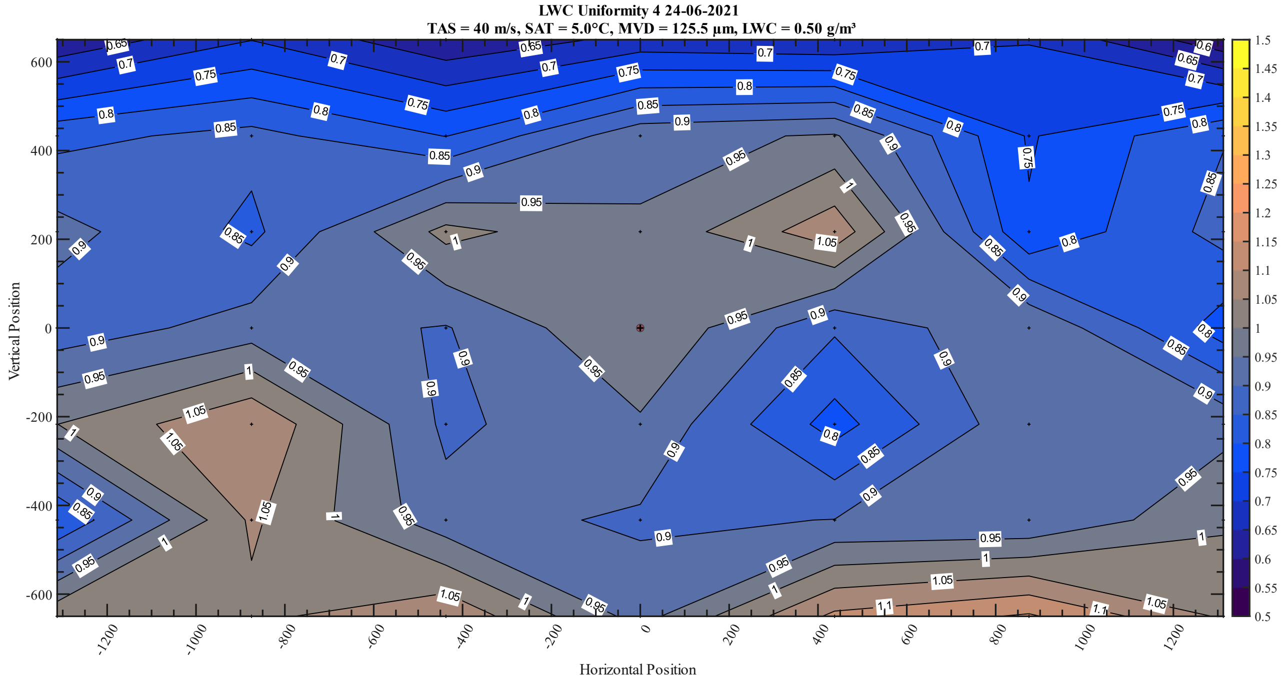

Figure 42: LWC Uniformity for the large mode of "FZDZ L4" at a test section airspeed of 40 m/s, test section mapping with Nevzorov Probe, spray bars 3-11 were active

4.4.7 PSD Uniformity

A mapping of the PSD has been performed with the CAPS probe form DLR. The resulting distributions are shown in Figure 43. In general, the measured MVD was very constant and remained within ±10% compared to the measured MVD in the centreline. The spot with the 25% higher MVD might be due to an issue with an individual nozzle, rather than a general non uniformity. No indication for a droplet size separation due to gravitational influences was observed for FZDZ MVD > 40 µm conditions.

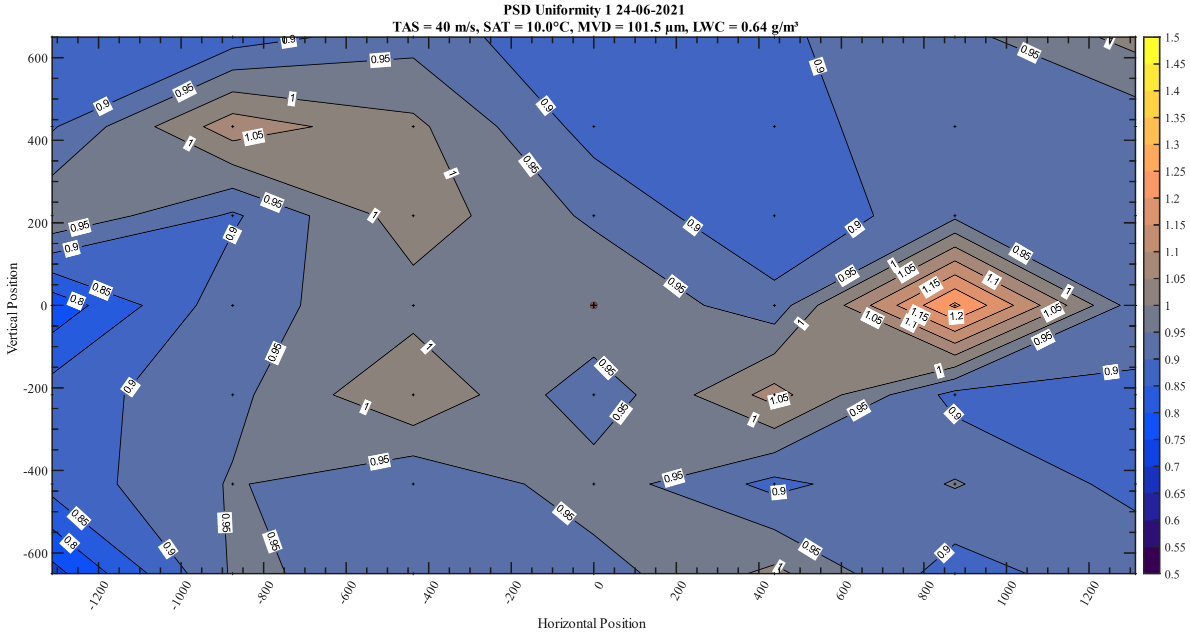

Figure 43: MVD Uniformity for "FZDZ L4" at a test section airspeed of 40 m/s, test section mapping with CAPS Probe, spray bars 3-11 were active

4.4.8 Droplet Temperature Measurement

Droplet temperature measurements have been performed by Rainbow Vision using their GRT-Mini instrument. The measurement has been performed with only the large mode of FZDZ L4 on both spray bar circuits active in order to increase the number of large droplets. The test section airspeed was set to 60 m/s at a SAT of -5°C. The measured water temperature in the spray nozzle supply lines was between 5°C and 8°C.

Figure 44 (left) shows a tri-modal Rosin-Rammler fit of the measured PSD, the measured MVD is in the region of 140 µm. In the right the recorded rainbow image from which the average temperature was derived is shown. An average droplet temperature of -4.1°C was measured for the large mode of the FZDZ MVD > 40 µm condition, which indicates a supercooled state of the large particles. This measurement confirms numerically obtained results.

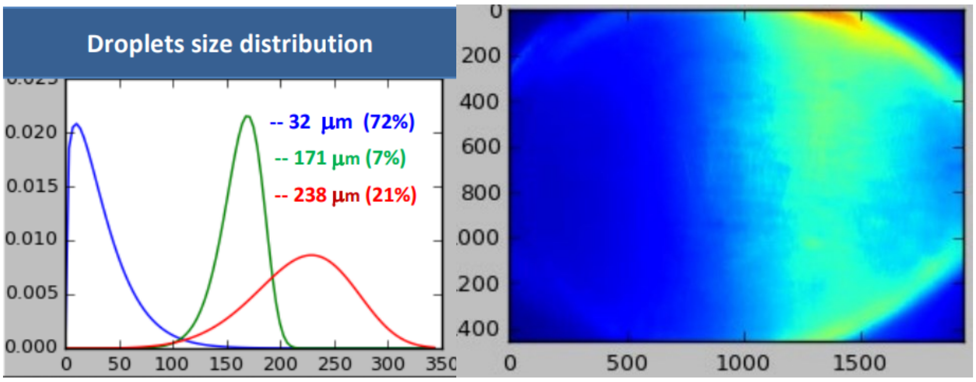

Figure 44: Example of validated measurement at RTA (for air temperature = -5°C, air velocity = 60 m/s, fitted PSD (left), recorded rainbow image (right)

4.4.9 Droplet Circularity

A rough estimation of the droplet circularity was derived from the CIP images obtained during the PSD measurements. A set of about 50 randomly selected droplets with equivalent diameters ranging from about 100 to 450 µm were analyzed using an algorithm implemented in the Matlab Image Processing Toolbox. Equation 9 shows how the circularity was calculated. In Figure 45 the resulting circularity values are listed. Circularities from 0.8 to ~1 were obtained, where 1 describes a perfect circle. Some values exceeded a circularity of 1, this is due to the uncertainty in the area and perimeter estimation. A slight trend towards more non perfect circles with increasing droplet sizes was identified.

$$Circularity = \frac{4 * \pi * Area}{Perimeter^2} \quad (9)$$

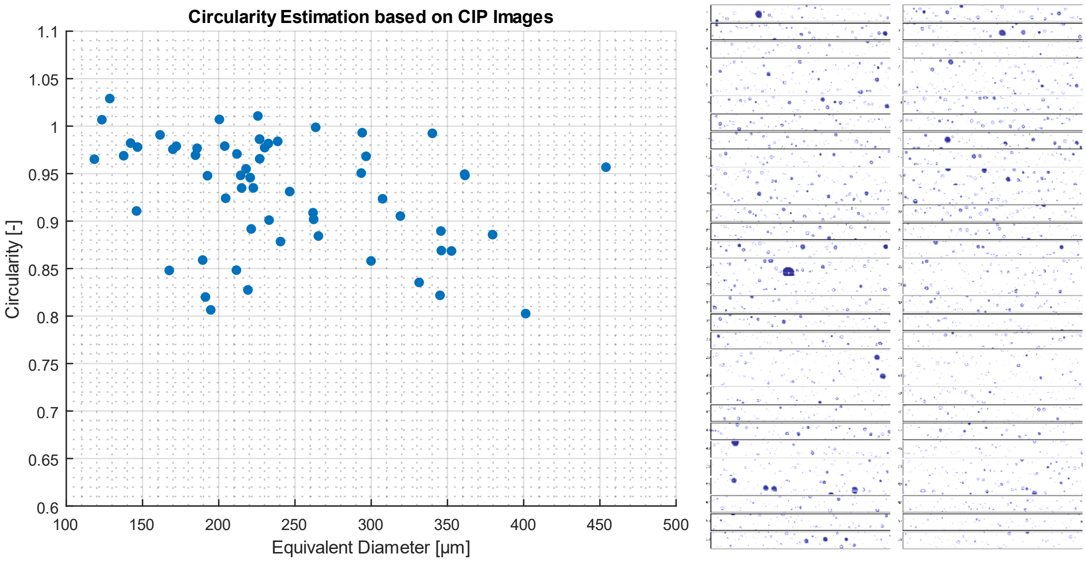

Figure 45: Circularity estimation based on CIP measurement results of FZDZ MVD > 40 µm

5 CIRA Icing Wind Tunnel

This facility has three interchangeable test sections and one open jet configuration. The aero-line with main internals and configurations is shown in Figure 46 with a table summarizing main performances. Some features are still unusual for large icing wind tunnel: downstream the fan diffuser, a twin row heat exchanger is also capable to control the air Relative Humidity (RH) before the spray bar, by means of a hot air compressor and steam injection. Controlled humidity ranges between 70% and 100% for temperatures between −15°C and −20°C. 100% humidity value can be set between −20°C and −40°C. Control accuracy is within ± 5% RH.

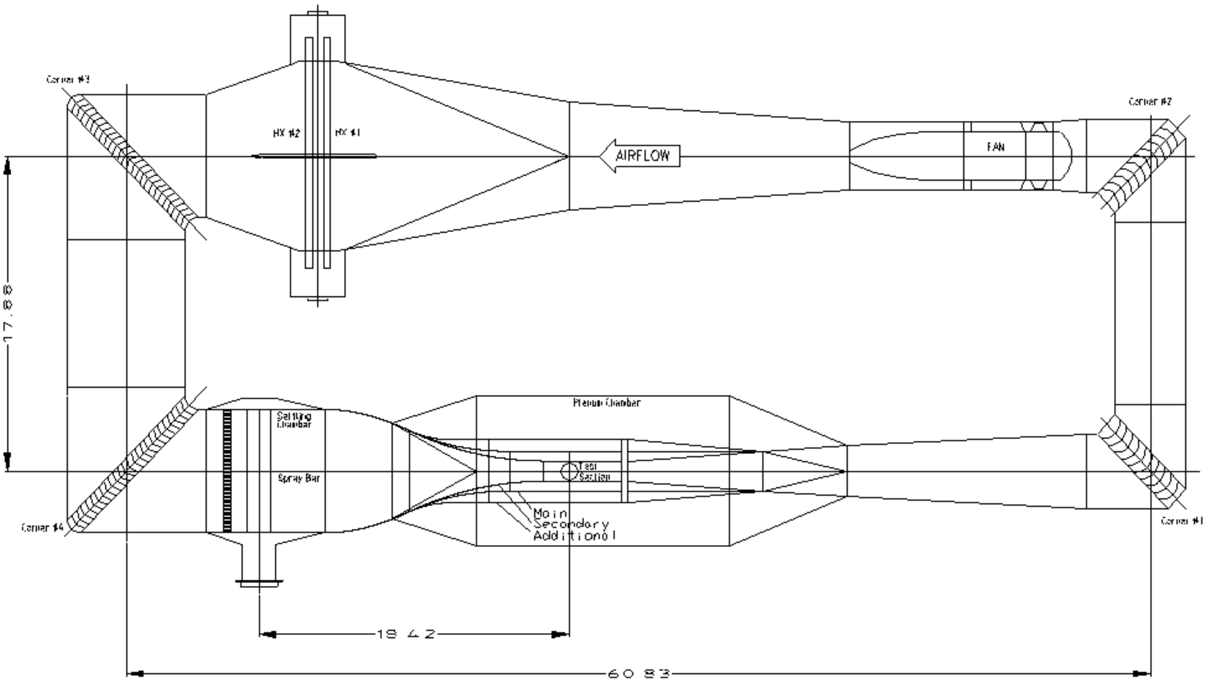

IWT configuration	Test section size (m)	Mach max	SAT (°C)	Altitude (m)
Main	2,25 x 2,35 x 7,0	0,41	-32° <T_s<+40°	up to 7000
Secondary	1,15 x 2,35 x 5,0 m	0,7	-40° <T_s<+40°	
Additional	3,60 x 2,35 x 8,3	0,25	-32° <T_s<+40°	
Open-jet	2,25 x 2,35 x 7,0	0,34	-32° <T_s<+40°	

Figure 46: CIRA Icing Wind Tunnel layout with main information on the test section configurations and performance

The facility settling chamber is fitted with a honeycomb module to reduce large scale eddies thus ensuring flow straightening. Downstream the honeycomb, an interchangeable section provides the possibility to switch the spray bar module with the screens module to improve the flow quality in the test section allowing the execution of the aerodynamic tests. A 0.7 MW centrifugal compressor unit allows the pressure to be regulated between 0.39 bars (corresponding to an altitude of 7000 meters) and 1.45 bars. While depressurization is used to simulate altitude for icing tests, pressurization, combined with a reduction in air temperature, helps to increase the Reynolds number for aerodynamic tests.

The SBS is located in the IWT stilling chamber, about 18 meters upstream the centre of test section, thus assuring a droplet residence time higher enough to achieve super-cooling conditions even for large droplet sizes. The SBS has 20 bars having a low drag aerodynamic shaped section, whose main feature is a low sensitivity to flow separation. Each bar is removable and may be vertically adjusted for optimising cloud coverage and uniformity, if necessary, during the calibration phase. Two spray nozzle types, one for small droplet spray and another for large droplet spray at the same air and water pressure settings, were selected to produce low LWCs to define an SLD envelope as close as possible to the Appendix O requirement for expected airspeed range. The two spray nozzle types were installed on each bar alternately until they covered its central section with up to 30 spray nozzles that can be remotely and independently activated through a solenoid valve using the same air and water manifolds for both. Thirty of twenty spray bars were used during the calibration, changing the number of operating spray nozzles on the base of condition (LWC and cloud uniformity) to reproduce by Facility Management System Software. Therefore, the SBS may use a single spray nozzle type (up to 15 per bar) to reproduce one PSD mode (small PSD-mode or large PSD-mode) or both spray nozzle types for bi-modal PSD clouds. The last SBS configuration can operate using the same air and water pressure settings for all the bars, taking advantage of different spray plume characteristics to generate bi-modal clouds. Another modality to operate using this configuration of the SBS is to set different air and water pressures to the odd bars with respect to the even bars. With this modality, water mass may change independently for each mode forming the PSD of the bimodal clouds.

5.1 Feasibility Study

Before to proceed with cloud calibration, to predict the behaviour of the SBS with different configurations, a simulation model was built considering the CIRA-IWT test-leg geometry (Figure 47). This model was based on Ansys-Fluent limited to the CIRA-IWT test leg with the spray bar configuration setting with two types of spray nozzles to generate bi-modal cloud condition at 110 ms^{-1} have been studied. A model with more than 12x10^{6} of polyhedral cells has been developed to study the effect of modified spray bar parameters and spray nozzles layout on main cloud proprieties in the test section (e.g., droplets' trajectories, droplets' temperature, droplet diameters distributions).

Results have shown the possibility to predict potential overlap of water mass in the reference area of the test section due to large droplets trajectories which amplitude depends of the spray nozzle plume angle combined by location of the spray nozzle on the spray bar. The simulation of the internal flow profiles for both velocity and water volume fraction have been studied for each spray nozzle types to predict the spray plume angle for representative air/water pressures. Results have been combined with experimental characterization of each spray nozzle type for a series of air/water pressures that provide the droplet diameter statistics. The measurements have been used for building the PSDs based on the Rosin-Rammler (RR) distributions for CFD input. These distributions with information on the spray plume angle has been used as boundary conditions for the simulation of droplet trajectories by injecting water droplets in the settling chamber by each spray nozzle, considering in the simulation the portion of the spray bar system reported in yellow rectangle of the Figure 47. Figure 48 shows the two phases of the simulation with an indication of typical results achievable for different spray nozzle grids on the spray bar array selected for this study.

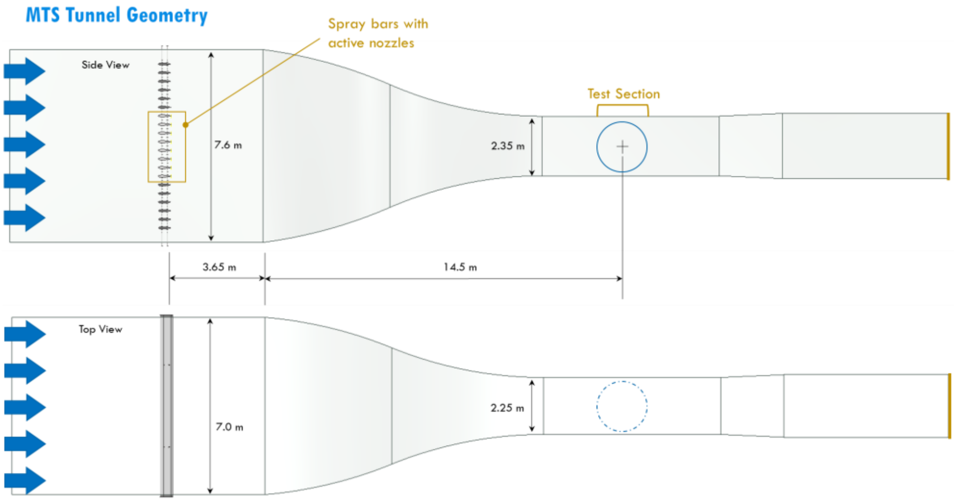

Figure 47: CIRA-IWT sketch showing the geometry considered for the CFD simulation with the test lag of the MTS configuration and the SBS.

The model predicts how far specific condition could be by uniform distribution of the main cloud parameters in the test section, including the water droplet temperature, showing for each condition the estimated cumulative volume fraction and normalized volume distribution (Figure 48).

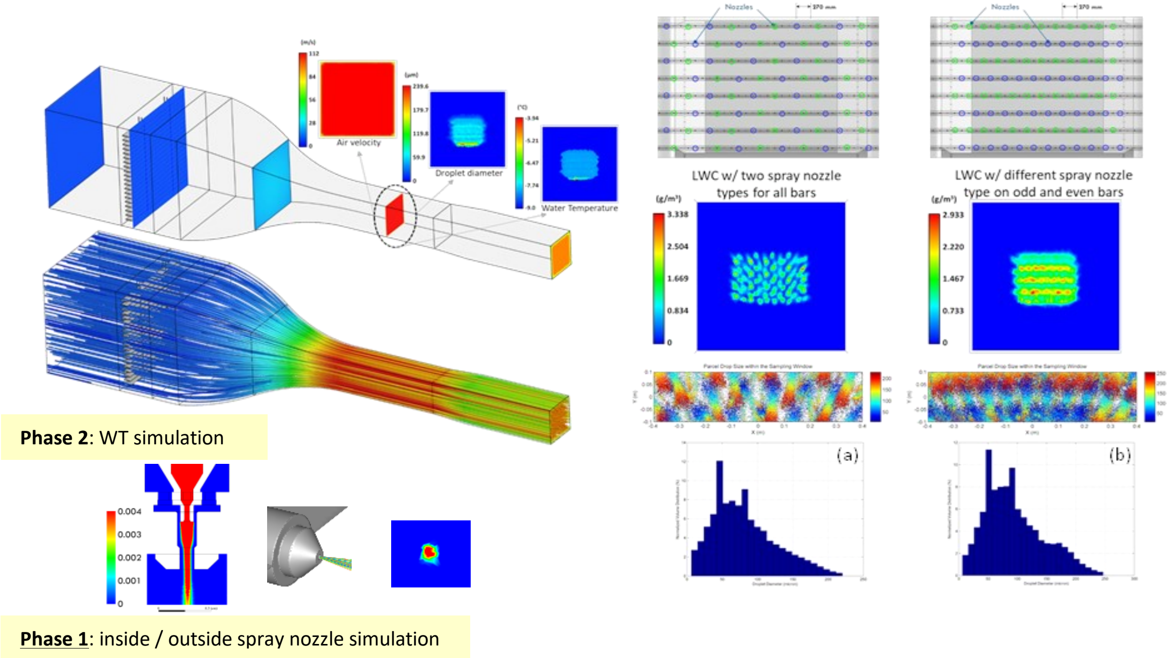

Figure 48: Study of the spray bar performance when equipped with two spray nozzle types. The first phase of this study analyses the main bi-phase flow parameters inside and outside each spray nozzle type. The simulation of the cloud inside the IWT test leg duct (phase 2) includes the assessment of LWC homogeneity with indication of potential PSD (normalized volume distribution) modifications due to different spray nozzle patterns on the spray bar module: (a) The two type of the spray nozzles are alternating on each bar; (b) each bar has a different spray nozzle (the even bars are those that produce large drops, and the odd bars are those that produce the smaller drops).

Results showing how may change the LWC distribution in the test section based on different SBS configuration and the estimated water droplet temperature achieved based on airflow conditions (droplet residence time). The example in Figure 48, shows the parcel drop size within the sampling window of the SBS for the mono-modal PSD (Figure 48a) at 0.7 gm^{-3} of LWC, and 180 μm of MVD. This condition changing when the odd bars of the SBS are limited to injects the smaller droplets of the PSD and the even bar the large one is set to generate the bi-modal clouds resulting in higher value of LWC achieving 1.17 gm^{-1} with 134 μm of MVD. These comparisons have been done at 110 ms^{-1}

5.2 SBS Configurations and Rationale for the Matrix of Cloud Conditions

The SLD cloud generation has been characterized using different Spray Bar System (SBS) configurations equipped with a different density of active spray nozzles that range from 130 to 195 in function of the target values of LWC and cloud uniformity to achieve in the tests section. The SLD improvement was achieved for CIRA-IWT, selecting a new water atomizer for better cloud uniformity and coverage area in the test section for the lower LWC values than the previous SBS configuration equipped with the spray nozzle with a single jet. The new atomizer operates with multi-jet spray to increase the spray plume angle to cover a larger cross section of the spray bar when the low LWC value to target requests a reduced number of active spray nozzles. To generate the Appendix O clouds limited to the FZDZ conditions with MVD below or higher than 40 μm and the Appendix C cloud conditions, 13 bars (from bar#4 to bar#16), each equipped with 30 spray nozzles, have been suited on the SBS for fast change from Appendix C to Appendix O. The total of 390 spray nozzles was symmetrically distributed in the cross-section of the settling chamber to limit the effect on the cloud uniformity passing from Appendix O to Appendix C *(gravitational effects on large droplet trajectories).* The two types of spray nozzles have been alternatively installed in each spray bar (from spray bar position 11 to spray position 40), allowing the change of the SBS configuration through the remote activation of the solenoid valve in each spray nozzle to turn the water flow in or off for each one. The Table 8 below reports the description of the SBS configuration in use with the number of active spray nozzles, the spray nozzle type, and the number of conditions tested for each SBS configuration. The first column provides a code name for each spray bar configuration used in the matrix of conditions. The objective was to explore the full potentiality of the SBS equipped with the new nozzle type in combination with the available single-jet spray nozzle to produce a bimodal spray at low LWCs.

ID_SBS configuration	**Single-jet SN** # of active spray	**Multi-jet SN** # of active spray	**Even bars** # of active spray	**Odd bars** # of active spray	**PSD / MVD** meas. points (#)	**LWC** meas. points (#)
1A2_SLD2	195	0	105	90	38	102
1A2_SLD3	0	195	105	90	10	8
1A2_SLD5	90	105	105	90	28	47
1A3_SLD6	65	65	5	5	13	9

Table 8: Spray bar system configurations with the indication of the type and number of active spray nozzles in use during the PSD/MVD and LWC measurements at the center of the test section.

Figure 49 shows an example of a comparison between the two spray nozzles at the same air/water pressure settings using a Laser Sheet Imaging (LSI) method to measure the intensity of the spray plume showing different spray concentration distribution in terms of size, shape and relative distribution of the spray plume at the same distance from the nozzle exit. Measurements were performed by Spraying Systems & Co. in ambient conditions using their open circuit aerodynamic wind tunnel by installing in the test section spray nozzle to study the spray plume characteristics when submitted at the same airspeed of the CIRA-IWT settling chamber (10 ms^{-1}).

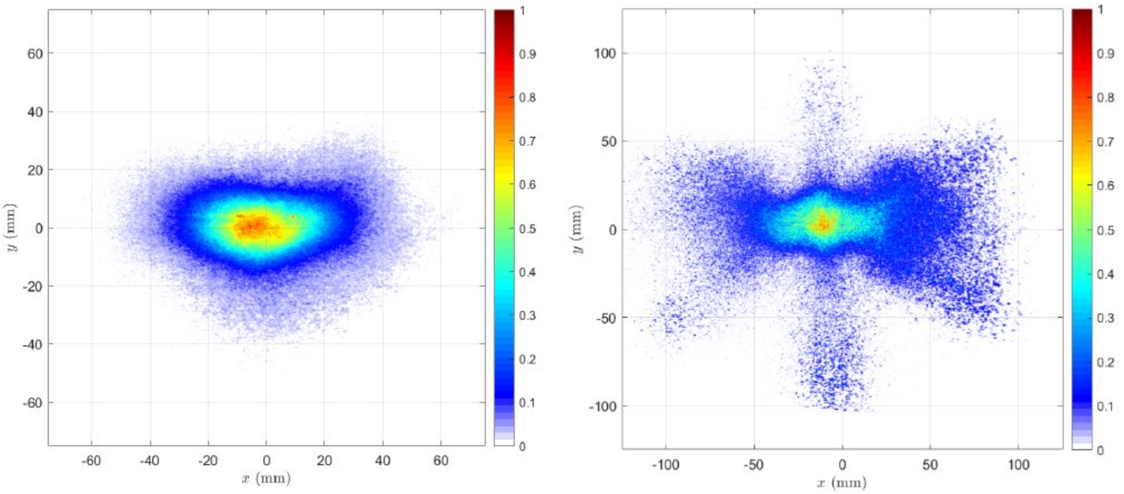

Figure 49: Water spray concentration measured by LSI system in the spray plume generated by single-jet (on the left) and multi-jet (on the right) spray nozzle.

The last two SBS configurations shown in Table 8, 1A2_SLD5 and 1A2_SLD6, 1A2_SLD5 and 1A2_SLD6, have been tested to measure the potential capability to generate the bi-modal PSD. For the first one, the air and water pressure settings of the even bars were chosen to produce large droplets, while the pressure settings of the odd bars were chosen to produce small droplets. In this configuration, the capability to modulate the mass flow, whether for a small or large size range, determines the degree of variability of the small and large modes in the bi-modal PSD. The last SBS configuration, 1A3_SLD6, has been used by setting all the bars at the same water and air pressures and using different spray nozzle features to generate small and large particles from the same bar. The total number of spray nozzles has been reduced for this configuration to allow the generation of clouds at lower LWC.

The following sections describe the measurement executed for each configuration of the SBS and the results obtained with this first part of CIRA-IWT cloud characterization.

5.3 PSD/MVD Measurements and Preliminary Results for FZDZ Conditions

The measurements activities in the CIRA-IWT were planned to a single slot from April 2022 to early June 2022 with the objective to collect enough data to support WP8 test campaign, just after the calibration activities. For this reason, not enough condition points were measured to collect a valid number of statistical data to determine general calibration curves for MVD/PSD to correlate with LWCs data.

5.3.1 PSD/MVD Test Matrix

The test matrix has been defined considering the cloud conditions based on past air and water pressure settings already tested in CIRA-IWT with the single-jet spray nozzle. For the airflow, the conditions were based on the requirements foreseen for theWP8 test campaign to be performed just after the end of the measurements of CIRA-IWT cloud calibration. For this reason, the flow conditions were defined for two airspeeds and three pressure altitudes. The matrix below (Table 9) reports all the airflow and SBS settings used during the measurements with DLR CCP probe from May 3rd to May 5th, 2022. The column "PSD mode" identifies the shape of the particle spectrum and the symbol (?) unstable cloud conditions that need further investigation/measurements.

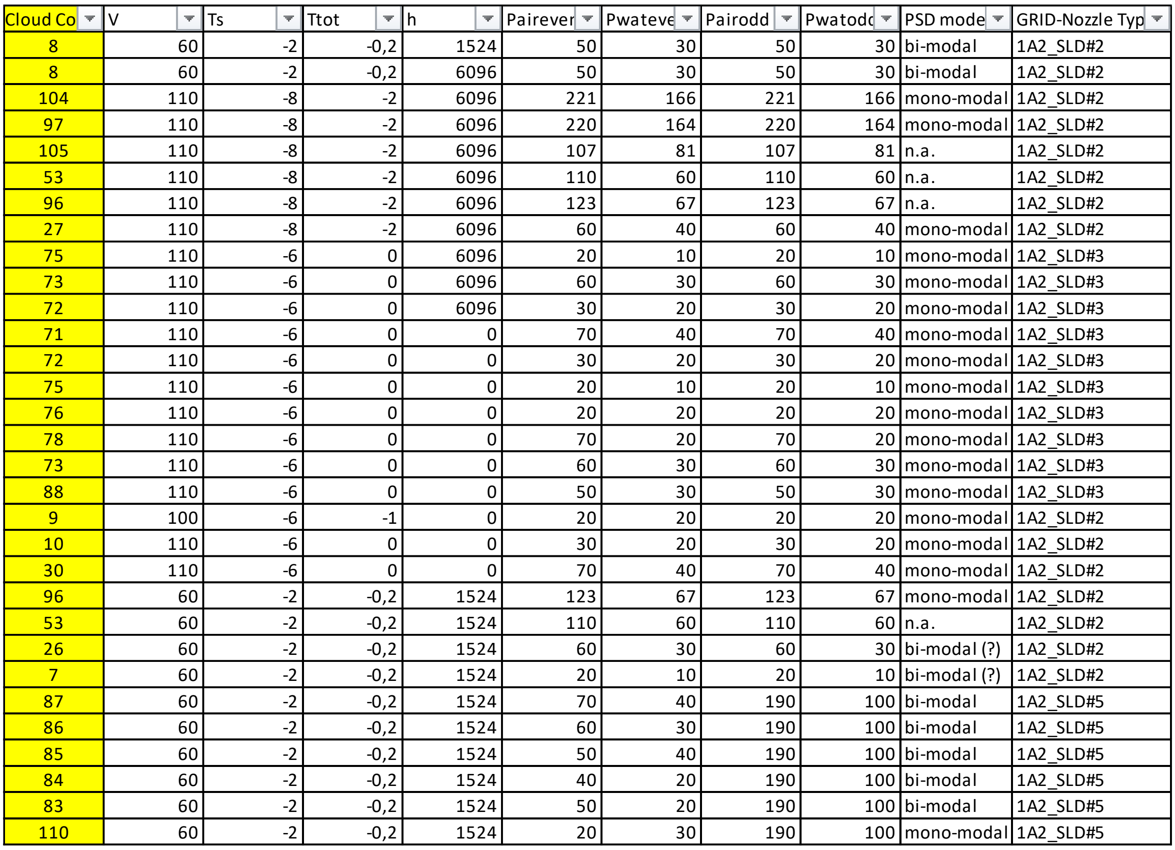

Cloud Co	V	Ts	Ttot	h	Pairever	Pwateve	Pairodd	Pwatod	PSD mode	GRID-Nozzle Typ
8	60	-2	-0,2	1524	50	30	50	30	bi-modal	1A2_SLD#2
8	60	-2	-0,2	6096	50	30	50	30	bi-modal	1A2_SLD#2
104	110	-8	-2	6096	221	166	221	166	mono-modal	1A2_SLD#2
97	110	-8	-2	6096	220	164	220	164	mono-modal	1A2_SLD#2
105	110	-8	-2	6096	107	81	107	81	n.a.	1A2_SLD#2
53	110	-8	-2	6096	110	60	110	60	n.a.	1A2_SLD#2
96	110	-8	-2	6096	123	67	123	67	n.a.	1A2_SLD#2
27	110	-8	-2	6096	60	40	60	40	mono-modal	1A2_SLD#2
75	110	-6	0	6096	20	10	20	10	mono-modal	1A2_SLD#3
73	110	-6	0	6096	60	30	60	30	mono-modal	1A2_SLD#3
72	110	-6	0	6096	30	20	30	20	mono-modal	1A2_SLD#3
71	110	-6	0	0	70	40	70	40	mono-modal	1A2_SLD#3
72	110	-6	0	0	30	20	30	20	mono-modal	1A2_SLD#3
75	110	-6	0	0	20	10	20	10	mono-modal	1A2_SLD#3
76	110	-6	0	0	20	20	20	20	mono-modal	1A2_SLD#3
78	110	-6	0	0	70	20	70	20	mono-modal	1A2_SLD#3
73	110	-6	0	0	60	30	60	30	mono-modal	1A2_SLD#3
88	110	-6	0	0	50	30	50	30	mono-modal	1A2_SLD#3
9	100	-6	-1	0	20	20	20	20	mono-modal	1A2_SLD#2
10	110	-6	0	0	30	20	30	20	mono-modal	1A2_SLD#2
30	110	-6	0	0	70	40	70	40	mono-modal	1A2_SLD#2
96	60	-2	-0,2	1524	123	67	123	67	mono-modal	1A2_SLD#2
53	60	-2	-0,2	1524	110	60	110	60	n.a.	1A2_SLD#2
26	60	-2	-0,2	1524	60	30	60	30	bi-modal (?)	1A2_SLD#2
7	60	-2	-0,2	1524	20	10	20	10	bi-modal (?)	1A2_SLD#2
87	60	-2	-0,2	1524	70	40	190	100	bi-modal	1A2_SLD#5
86	60	-2	-0,2	1524	60	30	190	100	bi-modal	1A2_SLD#5
85	60	-2	-0,2	1524	50	40	190	100	bi-modal	1A2_SLD#5
84	60	-2	-0,2	1524	40	20	190	100	bi-modal	1A2_SLD#5
83	60	-2	-0,2	1524	50	20	190	100	bi-modal	1A2_SLD#5
110	60	-2	-0,2	1524	20	30	190	100	mono-modal	1A2_SLD#5

25	60	-2	-0,2	6096	60	20	60	20	n.a.	1A2_SLD#2
26	60	-2	-0,2	6096	60	30	60	30	bi-modal	1A2_SLD#2
27	60	-2	-0,2	6096	60	40	60	40	bi-modal	1A2_SLD#2
9	60	-2	-0,2	6096	20	20	20	20	mono-modal	1A2_SLD#2
96	60	-2	-0,2	6096	123	67	123	67	mono-modal	1A2_SLD#2
97	60	-2	-0,2	6096	220	164	220	164	mono-modal	1A2_SLD#2
83	60	-2	-0,2	6096	50	20	190	100	bi-modal	1A2_SLD#5
84	60	-2	-0,2	6096	40	20	190	100	bi-modal	1A2_SLD#5
85	60	-2	-0,2	6096	50	40	190	100	bi-modal	1A2_SLD#5
86	60	-2	-0,2	6096	60	30	190	100	bi-modal	1A2_SLD#5
87	60	-2	-0,2	6096	70	40	190	100	bi-modal	1A2_SLD#5
110	60	-2	-0,2	6096	20	30	190	100	mono-modal	1A2_SLD#5
99	110	-6	0	1524	301	207	301	207	mono-modal	1A2_SLD#2
97	110	-6	0	1524	220	164	220	164	mono-modal	1A2_SLD#2
100	110	-6	0	1524	129	86	129	86	n.a.	1A2_SLD#2
96	110	-6	0	1524	123	67	123	67	n.a.	1A2_SLD#2
53	110	-6	0	1524	110	60	110	60	n.a.	1A2_SLD#2
98	110	-6	0	1524	123	50	123	50	n.a.	1A2_SLD#2
127	110	-6	0	6096	20	30	301	207	bi-modal	1A2_SLD#5
85	110	-6	0	6096	50	40	190	100	bi-modal	1A2_SLD#5
86	110	-6	0	6096	60	30	190	100	bi-modal (?)	1A2_SLD#5
87	110	-6	0	6096	70	40	190	100	bi-modal	1A2_SLD#5
26	110	-6	0	6096	60	30	60	30	mono-modal	1A2_SLD#2
25	110	-6	0	6096	60	20	60	20	mono-modal	1A2_SLD#2
9	110	-6	0	6096	20	20	20	20	mono-modal	1A2_SLD#2
26	110	-6	0	1524	60	30	60	30	mono-modal	1A2_SLD#2
41	110	-6	0	1524	70	50	70	50	mono-modal	1A2_SLD#2
13	110	-6	0	1524	160	70	160	70	n.a.	1A2_SLD#2
3	110	-6	0	1524	160	80	160	80	mono-modal	1A2_SLD#2
90	110	-6	0	1524	160	90	160	90	mono-modal	1A2_SLD#2
2	110	-6	0	1524	160	120	160	120	mono-modal	1A2_SLD#2
39	110	-6	0	1524	190	90	190	90	mono-modal	1A2_SLD#2
85	110	-6	0	1524	50	40	190	100	bi-modal	1A2_SLD#5
87	110	-6	0	1524	70	40	190	100	bi-modal	1A2_SLD#5
128	110	-6	0	1524	40	30	190	100	bi-modal	1A2_SLD#5
127	110	-6	0	1524	20	30	301	207	bi-modal	1A2_SLD#5
110	110	-6	0	1524	20	30	190	100	bi-modal	1A2_SLD#5
111	110	-6	0	1524	20	20	190	100	bi-modal	1A2_SLD#5
86	110	-6	0	1524	60	30	190	100	bi-modal	1A2_SLD#5
81	110	-6	0	0	20	20	20	20	mono-modal	1A3_SLD#6
82	110	-6	0	0	20	40	20	40	mono-modal	1A3_SLD#6
83	110	-6	0	0	50	20	190	100	bi-modal	1A2_SLD#5
84	110	-6	0	0	40	20	190	100	bi-modal	1A2_SLD#5
85	110	-6	0	0	50	40	190	100	bi-modal	1A2_SLD#5
86	110	-6	0	0	60	30	190	100	bi-modal	1A2_SLD#5
87	110	-6	0	0	70	40	190	100	bi-modal	1A2_SLD#5
80	110	-6	0	0	40	50	40	50	mono-modal	1A3_SLD#6
115	110	-6	0	0	30	20	30	20	mono-modal	1A3_SLD#6
116	110	-6	0	0	30	30	30	30	n.a.	1A3_SLD#6
117	110	-6	0	0	30	90	30	90	n.a.	1A3_SLD#6
118	110	-6	0	0	40	20	40	20	n.a.	1A3_SLD#6
119	110	-6	0	0	40	30	40	30	mono-modal	1A3_SLD#6
120	110	-6	0	0	50	20	50	20	n.a.	1A3_SLD#6
121	110	-6	0	0	50	30	50	30	mono-modal	1A3_SLD#6
123	110	-6	0	0	50	40	50	40	n.a.	1A3_SLD#6
124	110	-6	0	0	60	30	60	30	bi-modal	1A3_SLD#6
125	110	-6	0	0	60	40	60	40	n.a.	1A3_SLD#6
8	110	-6	0	1524	50	30	50	30	n.a.	1A2_SLD#2

Table 9: Matrix of cloud conditions (in the first column) used during the PSD/MVD cloud characterization with DLR CCP probe.

5.3.2 PSD/MVD Results from Preliminary SLD Calibration

The assessment of the FZDZ conditions in CIRA-IWT were mainly supported by DLR using the CCP probe (Figure 50), which is a combination of scattering technique, CDP with a 2 µm – 50 µm size range, and CIP-G probe, an Optical Array Probe with a 15 µm – 930 µm size range. CIRA 4D-PDI probe with size range 1µm – 698 µm has also been used during the measurements for low concentration cloud conditions.

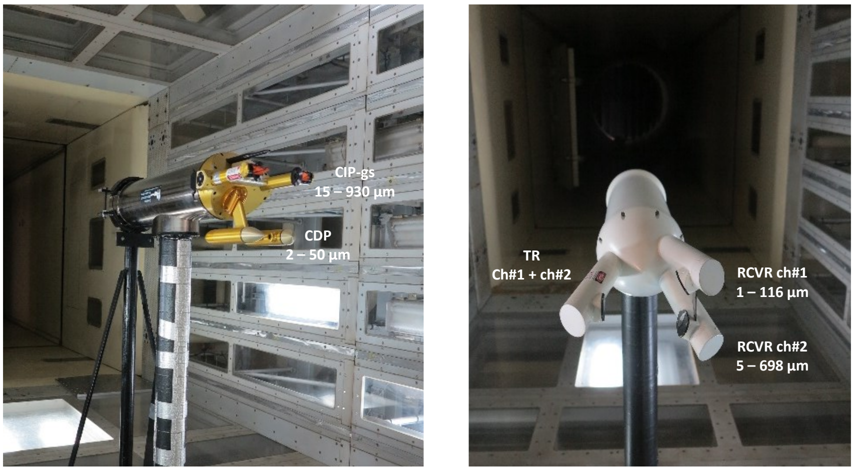

Figure 50: DLR CCP (Cloud Combination Probe) on the left, installed in the centerline of the CIRA IWT test section during the PSD/MVD measurement slot. CIRA 4D-PDI on the right installed with sample volume located on the centerline, in the same position of DLR CCP.

The measurements have been performed at the centre of rotation of the model support system after cloud uniformity check performed with icing cylinders.

Figure 51 to Figure 54 shows the features of each spray bar configuration to generate clouds for some conditions close to the FZDZ cumulative volume fractions curves for MVD below and higher than 40 µm at low liquid water content values. Some other conditions are far from target PSD requirement and this is manifested by the fact of data processing and analysis has not been followed by a second measurement slot with adjusted air/water pressure settings. What has been learned from these first results is how the influence of the SBS configurations (spray nozzle types ratio) is sensitive to the facility's target requirements (Appendix O).

In Figure 51, the resulting PSDs are compared with the reference cumulative volume fraction described in Appendix O. Cloud conditions are generated using the single-jet spray nozzle with the spray bar configuration 1A2_SLD2.

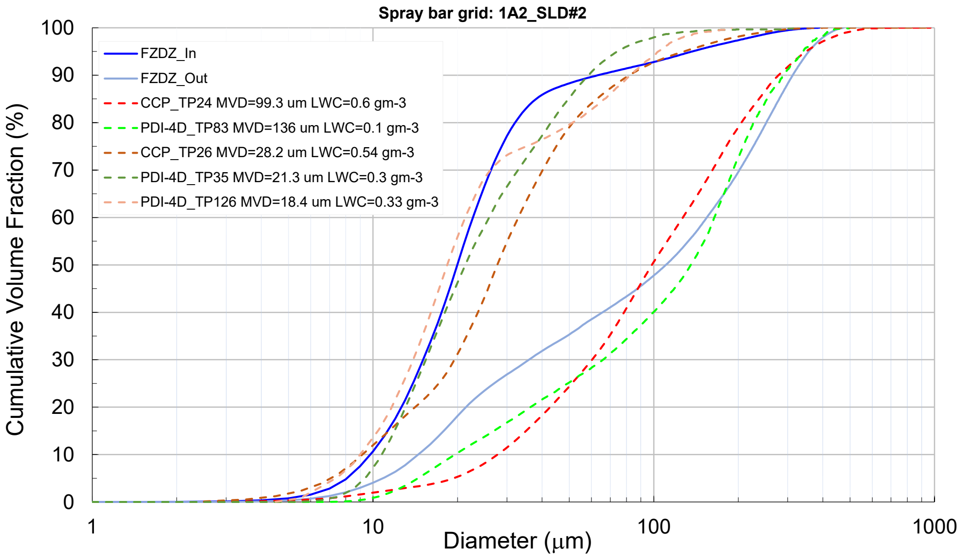

Figure 51: Cumulative volume fraction measured by CCP and 4D-PDI at 110 ms-1 measured with 1A2_SLD2 of SBS configuration.

The three dashed curves collected by CCP and PDI-4D show some variability to agree with the full reference curve of FZDZ below the 40 μm from about 70% of cumulative volume fraction, even if the two 4D-PDI measurements are quite close below this value. For the cloud generated with this spray bar configuration, the data measured showed the MVD changes between 18.4 μm and 21.3 μm and LWC ranging from 0.3 to 0.54 gm^{-3}.

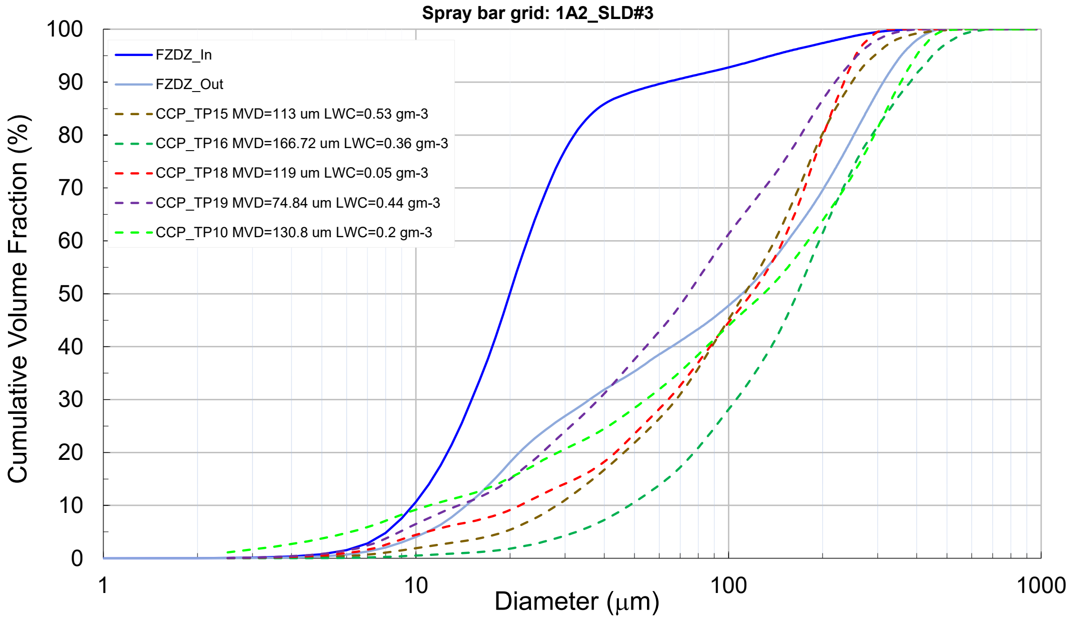

Figure 52: Cumulative volume fraction measured by CCP probe at 110 ms-1 measured with 1A2_SLD3 of SBS configuration.

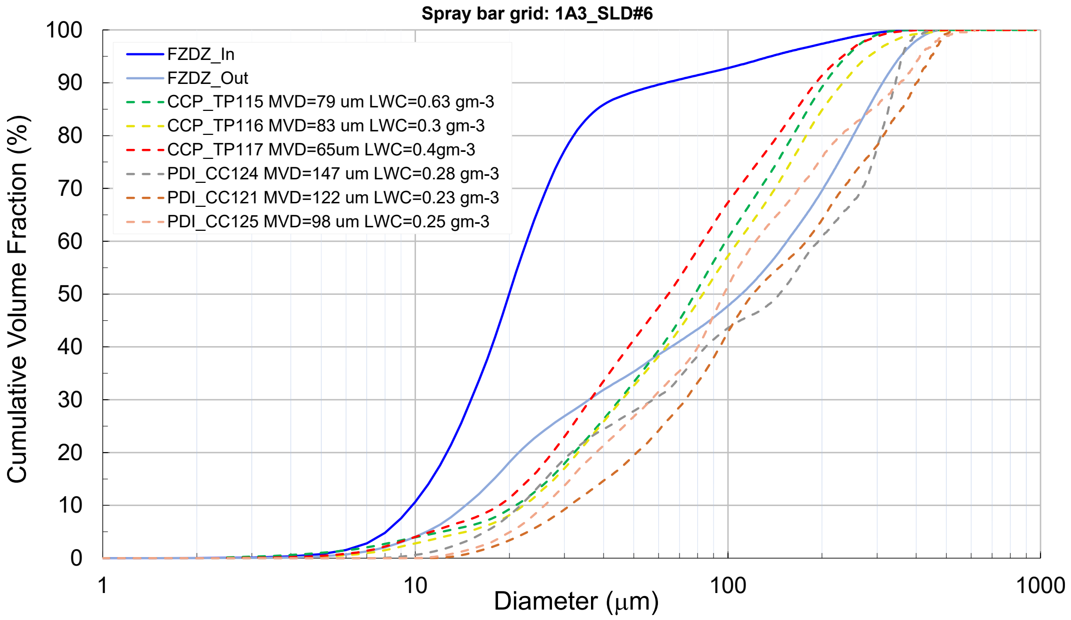

Figure 53: Cumulative volume fraction measured by CCP and PDI probe at 110 ms-1 measured with 1A3_SLD6 of SBS configuration.

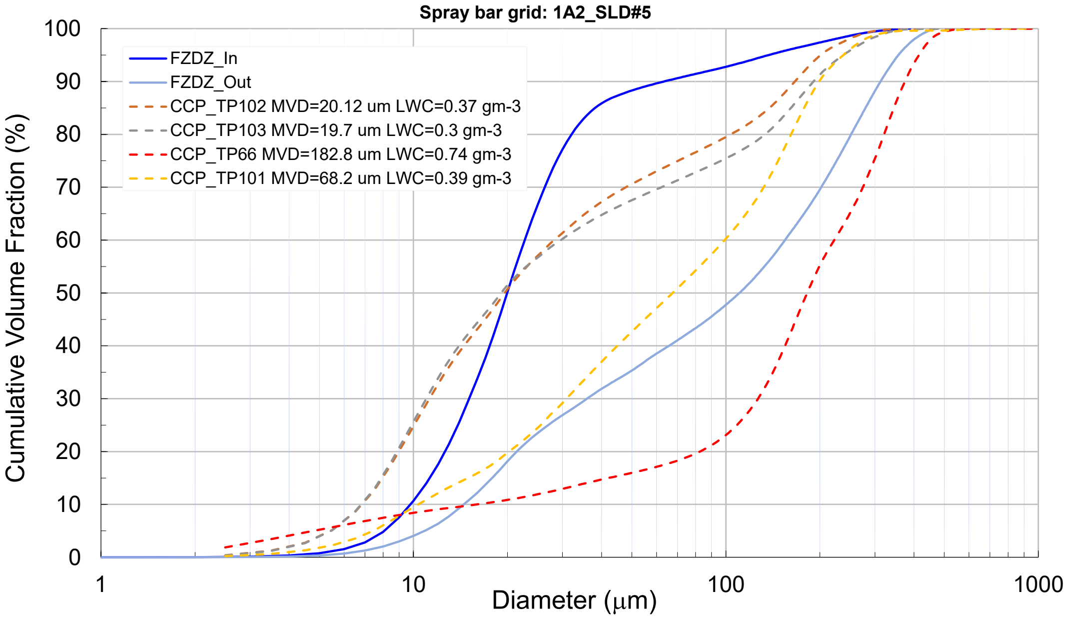

Figure 54: Cumulative volume fraction measured by CCP and PDI probe at 110 ms-1 measured with 1A2_SLD5 of SBS configuration.

In particular, the SBS with 1A2_SLD2 grid configuration equipped with single-jet spray nozzles allows the generation of low MVD at low LWC and provides most of the monomodal PSDs for both FZDZ envelopes. This configuration will be consistent with the values to achieve with FZDZ with MVD < 40 μm **(FZDZ-In)**. Considering the same number of active sprays, 195, using the multi-jet spray nozzles with 1A2_SLD3 spray bar grid configuration, the PSD shape becomes, for most of the conditions tested, bi-modal and close to the target PSDs for some conditions, as shown for the case of the test point 10 reported in Figure 52 as an example.

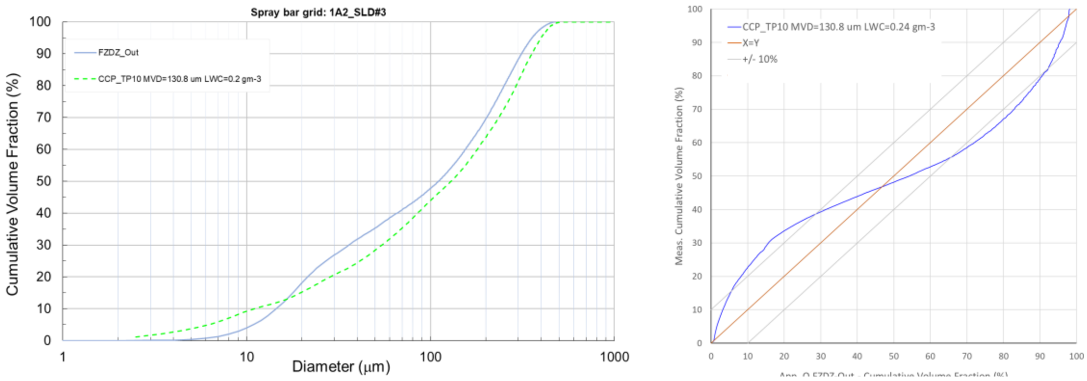

Figure 55: Example of the quantile-quantile plot showing the agreement between the measured PSD and Appendix O requirement with 1A2_SLD3 spray bar configuration. Data has been collected by CCP probe at 110 ms^{-1} and at pressure altitude of 6096 m.

To quantify the degree of agreement between reference PSD in Appendix O and test point 10, Figure 55 reports the quantile-quantile plot showing how their difference changes for the full diameter range within the uncertainty threshold determined by the PSD target requirement. For this cloud condition, the deviation from the reference PSD is almost outside by 10%, even if must be highlighted that small changes in the spray bar settings may influence the behaviour shown in Figure 55.

The SBS with 1A2_SLD3 grid configuration shows an advantage in changing the PSD shapes from mono-modal to bi-modal for the FZDZ with MVD>40μm **(FZDZ-Out)**. This configuration has limitations in generating the small droplets and, thus, difficulties in covering the envelope defined in the FZDZ-In. Despite the advantage of overlapping the FZDZ-Out, this SBS configuration shows some difficulties in maintaining the requested bi-modal PSD shape by changing the mass concentration for each of the two modes of PSD of FZDZ-Out requirement through the variation of the spray bar pressure settings, keeping the LWC within the target values (< 0.3 gm-3) for expected airspeed range (e.g., from 60 ms^{-1} to 120 ms^{-1}). At this end, the use of SBS with 1A3_SLD6 and the 1A2_SLD5 grid configurations (Figure 53 and Figure 54) are able to produce bi-modal PSDs at low LWC respectively with a medium and high level of controllability of small and large mode of the PSDs shapes.

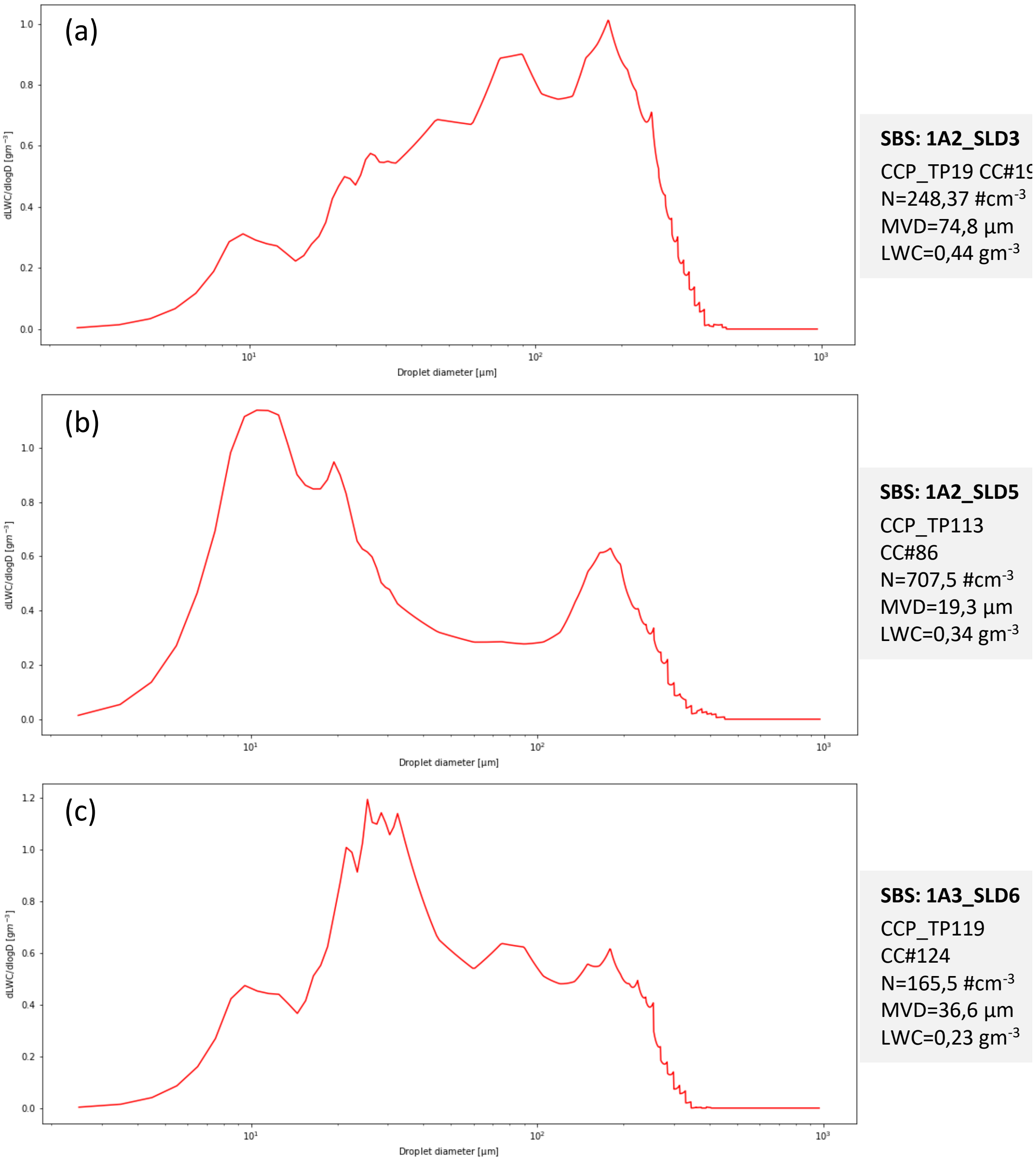

SBS: 1A2_SLD3
CCP_TP19 CC#1
N=248,37 #cm^{-3}
MVD=74,8 µm
LWC=0,44 gm^{-3}

SBS: 1A2_SLD5
CCP_TP113
CC#86
N=707,5 #cm^{-3}
MVD=19,3 µm
LWC=0,34 gm^{-3}

SBS: 1A3_SLD6
CCP_TP119
CC#124
N=165,5 #cm^{-3}
MVD=36,6 µm
LWC=0,23 gm^{-3}

Figure 56: Effect of the spray bar configurations on water mass distribution for the same condition: 110 ms-1 of airspeed with the SBS setting at the same air and water pressures (case a and c) excluding the case (b) with half spray nozzles setting at higher pressures to generate the smaller droplets.

An example of variability in the PSD shape is provided by Figure 54, which shows the sensitivity of the CIRA-IWT spray bar system with the dLWC/dlogD plots. The area below these plots represents the LWC of the artificial clouds generated with the air pressure at 60 kPa and the water pressure at 30 kPa for each spray bar configuration shown in this figure excluding the case of Figure 56 b, where only the even bars (105 multi-jet spray nozzles, see Table 8) are setting to the same air and water pressures to contribute for large droplets concentration in the cloud. Thus, the 1A2_SLD5 spray bar configuration has the same number (195) of active spray nozzles as the 1A2_SLD3, but almost half of active spray nozzles (90 with the single jet type) contribute to the concentration for the lower part of PSD diameter represented in the Figure 56 b. Therefore, by changing the air and water pressures only for the odd bars, the concentration of the small droplet diameter range in the PSD mode in Figure 56 b can be modified. PSD/MVD cloud calibration for FZDZ with such spray bar configuration requests an iterative measurement process that includes attempt data processing and analysis followed by an additional measurement section to finalize the full calibration at different flow conditions (airspeed and pressure altitude).

5.4 LWC measurements

Measurements have been performed at the center of rotation of the model support system with SEA WCM-2000 with multi-wire (MW) by using its total water content (TWC) sensing element and the Robust Probe (RP). The second hot-wire sensor agrees well with the MW and provides a more accurate measurement for larger MVD (> 200 µm) for assessing if some SBS settings are providing unexpected FZRA clouds [8]. Figure 57 shows the set-up of the RP during the measurement section. Up to 150 test points were collected during the measurements, most with the 1A2_SLD2 spray bar configuration to characterize the full LWC envelope at 110 ms^{-1} and sea level pressure altitude. The LWC for the other SBS configurations has been characterized only for some limited conditions for checking achievable LWC values.

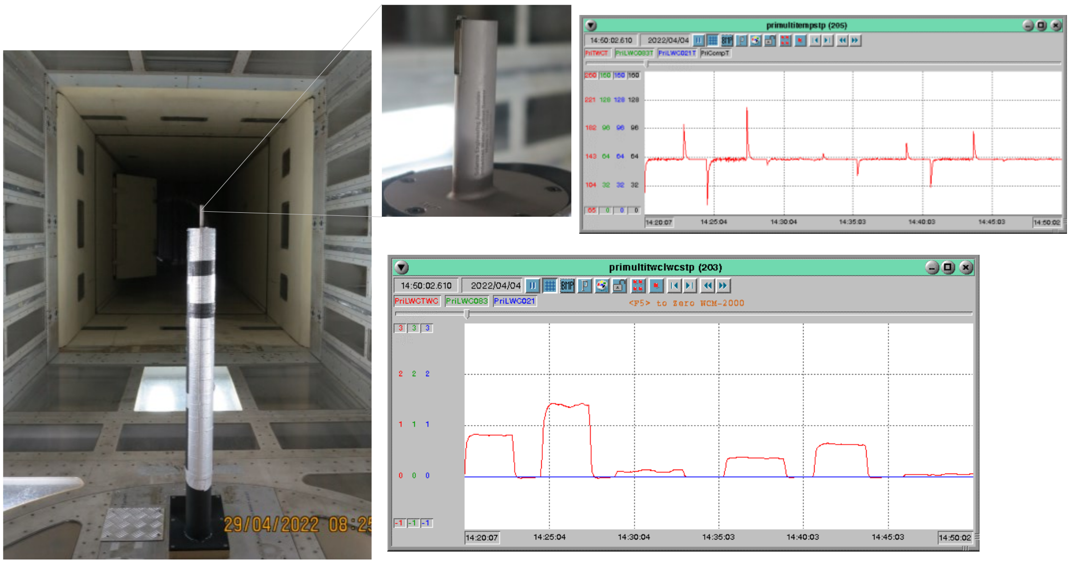

Figure 57: LWC measurements with RP installed on the strut to locate its sampling volume at the centerline of the CIRA-IWT test section. The plot on the top shows the sensor element temperature during the acquisition and between each test point. TWC behaviour for some conditions is shown in the bottom plot.

The collision efficiency is an important correction factor for hot-wire probes and has been determined on the base of sensing element geometry in agreement to the reference [8]. This parameter describes the impingement of water droplets due to their inertia, drag, and interaction with the aerodynamic flow field and do not include splashing and re-entrainment of droplets impacting the sensor, which can dominate net sensor efficiency especially for SLD. For each test point, an appropriate time average of the measurements to show stable values (e.g., 60, 90, or 120 seconds) have been collected at total air temperature below zero to prevent droplets re-circulation. The dry power response has been directly extracted by the sensing element taking a stable dry period when spray is not present. Between each spray point, the dry power value has been verified with LWC=0 g m^{-3} to ensure that neither droplet re-circulation nor ice formation on the sensing element or around the probe that may affect the accuracy of subsequent measurement points would occur.

For available measurement slot, only one SBS configuration, the 1A2_SLD2, have been characterized and results are shown in Figure 58.

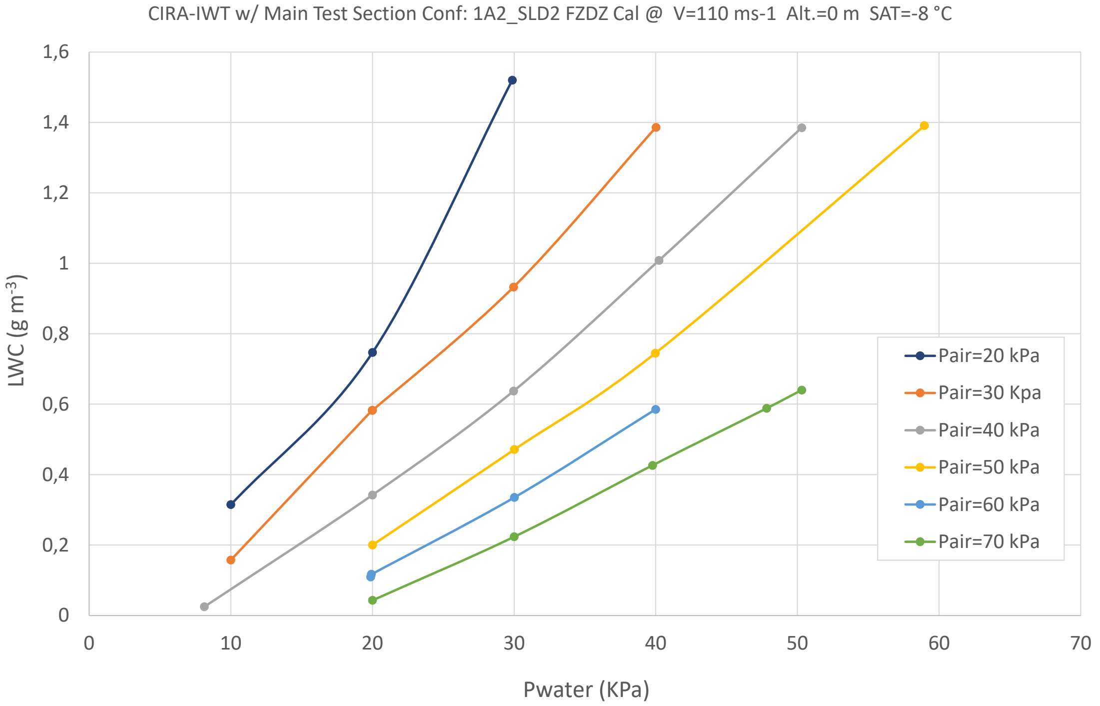

Figure 58: Cloud LWC calibration generated by 1A2_SLD2 spray bar configuration at 110 ms^{-1} and with pressure altitude at sea level.

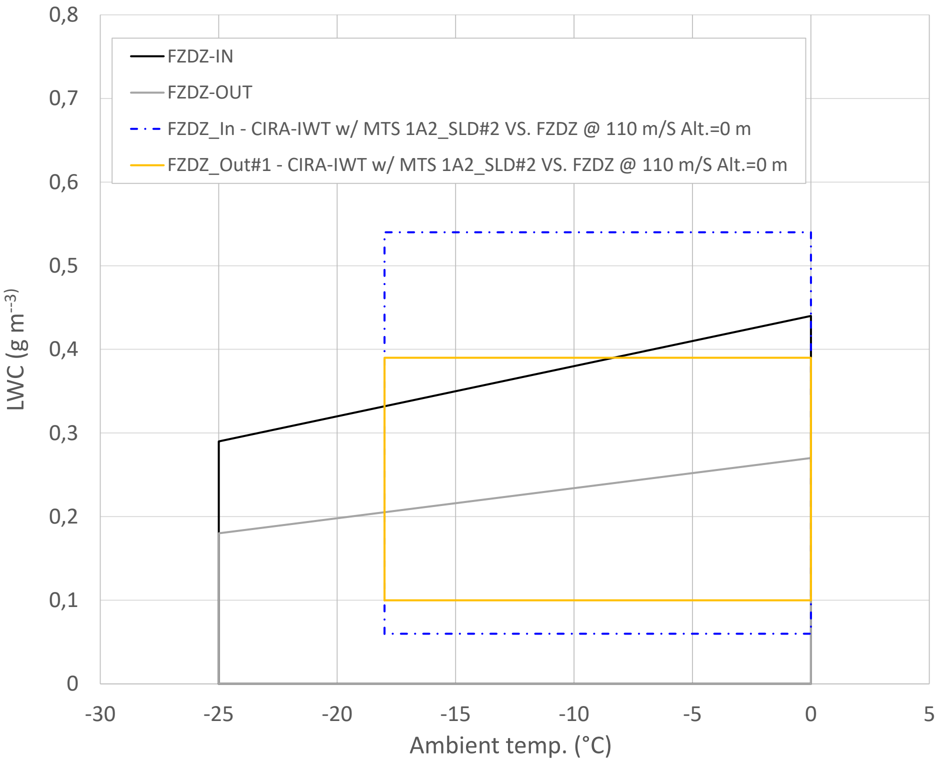

Figure 59: LWC calibration envelope for FZDZ cloud conditions generated by 1A2_SLD2 spray bar configuration

Data have been collected at -8 °C of air temperature, but the same conditions have been tested up to -18 °C. Figure 59 above compares the envelope covered by the same SBS configuration over a range of SAT with the FZDZ requirement. Further measurements with other SBS configurations must be performed considering the wide potentiality of improvement of the SLD cloud envelope in CIRA-IWT.

5.4.1 LWC uniformity

Preliminary assessment of cloud uniformity and coverage area in the reference plane at the centre of rotation of the model support system has been performed for each spray bar configuration at low, 60 ms^{-1}, and high speed, 110 ms^{-1}.

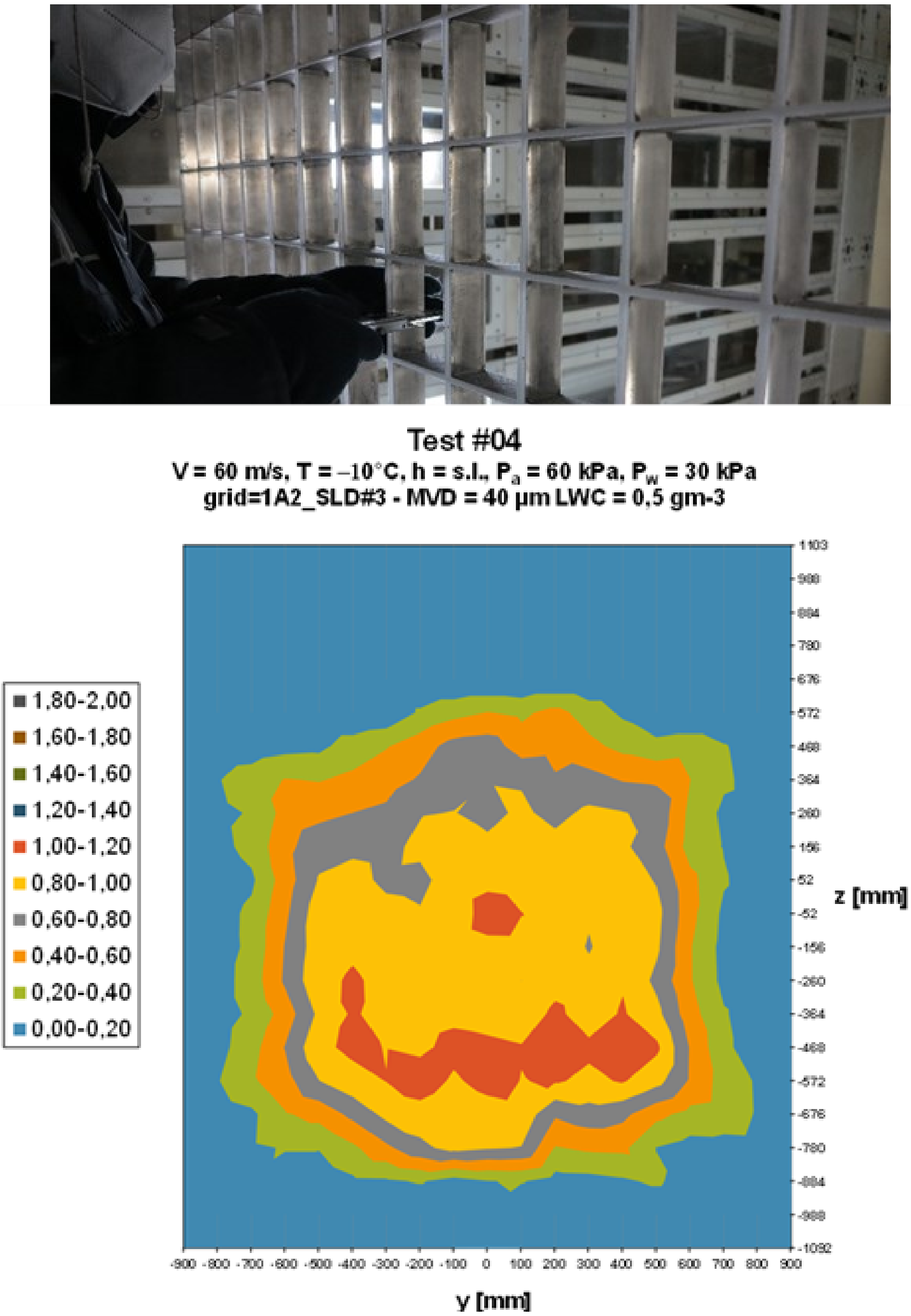

Figure 60: Cloud uniformity for one of the Appendix C conditions was measured with an Icing Grid at 60 ms-1 at sea level of pressure altitude. Cloud has been generated with 1A2_SLD3 spray bar configuration at minimum MVD.

For this task, both the Icing Calibration Grid (IG) and the Icing Cylinders (IC) method have been used. The first method mainly applied for the Appendix C, according to the guidelines of ARP 5905 (Aerospace Recommended Practice SAE ARP5905, Sept. 2015). At low MVDs, the IG will provide quantitative information on the local LWC and thus its spatial distribution through contour maps derived by using a dimensionless ratio of the LWC at a given location in the test section divided by the LWC at the centre of the test section. The LWCs are derived from ice thickness measurements at midpoints of vertical IG components. For the measured test cases, a good coverage and cloud uniformity in reference area have been found with expected LWC variation within±20% as shown the example reported in Figure 60. Figure 61 shows an example of the result achieved by cloud uniformity check for a typical Appendix O conditions with the ice thickness along the IC collected at 110 ms-1 for 110 µm of MVD and 0.5 gm-3 of LWC. The plot in Figure 61 highlights how the ice thickness values on the three cylinders, normalized to the centre value of the central cylinder, fall within the threshold limits of ±20%.

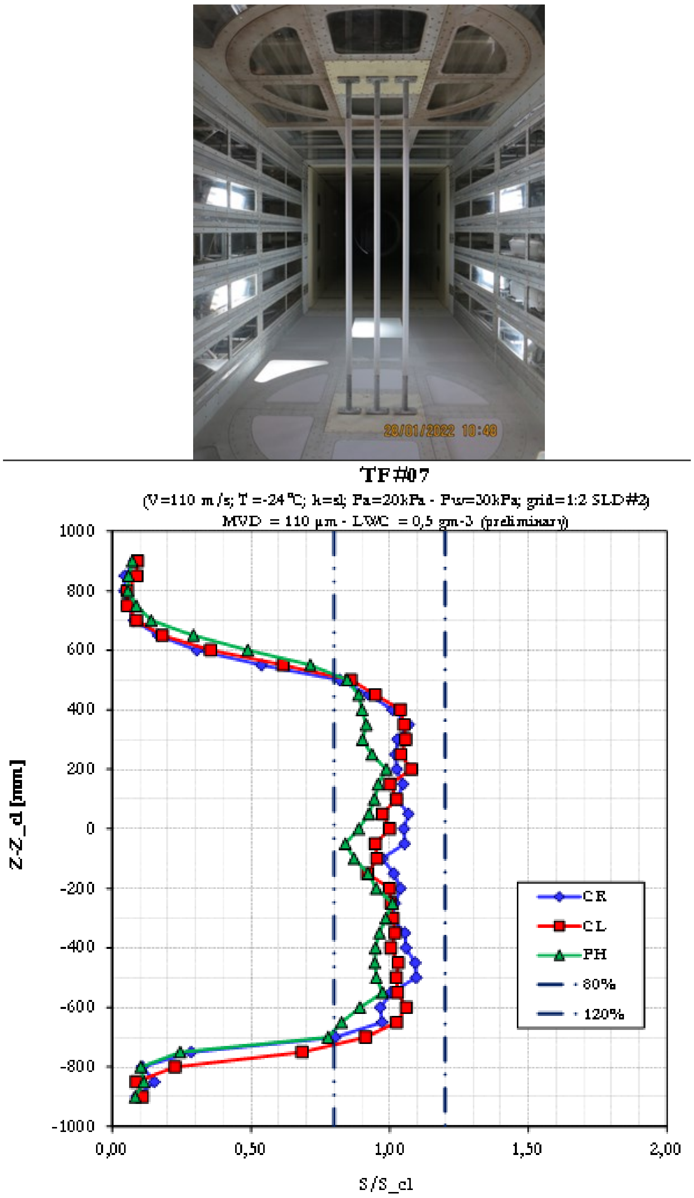

Figure 61: Variation of the ice thickness along the three cylinders located in the reference area of the test section. 1A2_SLD2 spray bar configuration has been used to generate 110 µm of MVD cloud with 0.5 gm-3 of LWC.

5.4.2 Droplet Temperature Measurement

The objective of measurements performed by Rainbow Vision using their GRT-Mini instrument, was to measure the temperature of large droplets inside the CIRA Icing Wind Tunnel for different cloud concentrations and distributions. As for the natural rainbow, results are based on the sum the rainbows signals scattering from several droplets passing through the probe volume providing the mean droplet refractive index that could be sensible to the droplet shapes if not properly “spherical”. The droplet temperature measurement is very difficult to achieve in the range of ± 5 °C due to not biunique relationship between the droplet refractive index and its temperature.

In May 2022, an upgraded version of GRT-Mini has been tested for the first time at CIRA. The GRT-Mini was installed horizontally inside the wind tunnel as shown in Figure 62. The measurement device is connected with the optical fibre and controlled from the control room at a distance of about 30 meters. A four-days measurement campaign has been carried out at CIRA from which one day using for setting up the device inside the IWT.

To validate GRT-Mini operation and adjustment, a successful calibration experiment has been carried out inside the CIRA IWT, by measuring the temperature and size distribution of a spray created by an ultrasonic nozzle. The temperature of the injected water was equal to the air temperature in the wind tunnel which was equal to about 15.3°C (with an air velocity equal to 0 m/s). Figure 62, is an example of recorded global rainbow signal. In this case, the measured average refractive index was equal to 1.3357 with a standard deviation equal to 0.00019 corresponding to a droplet temperature equal to ~15 °C with the standard deviation of about 2°C.

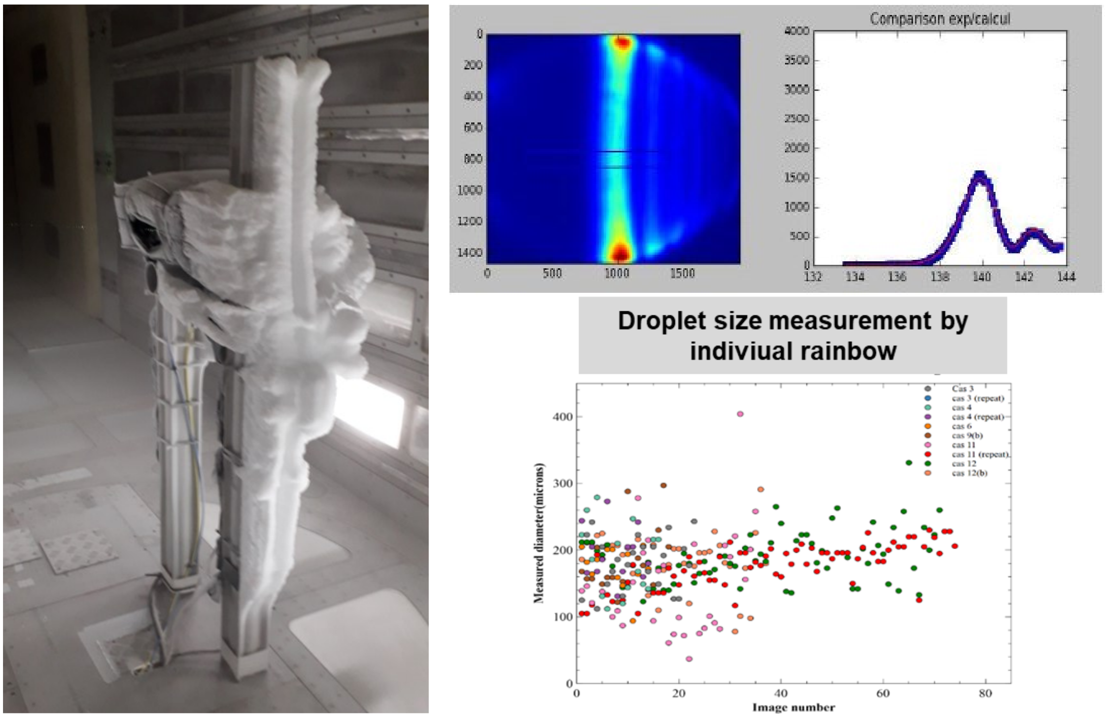

Figure 62: GRT-Mini probe layout in CIRA-IWT with ice contamination on its struct. An example of a global rainbow image with the associated angular light distribution for a spray created (on the right).

The CIRA wind tunnel airflow condition was set at 45 ms^{-1} , the maximum airspeed achievable for safe mechanical conditions of the probe strut, avoiding excessive vibration during the measurements amplified with the icing building up, with the static air temperature to -18°C. Several injection conditions have been selected by CIRA, with very low LWC, about 0.1 -0.58 g/m^3 shown in Table 10. Moreover, two different altitudes have been simulated, 1524 and 6000 m respectively.

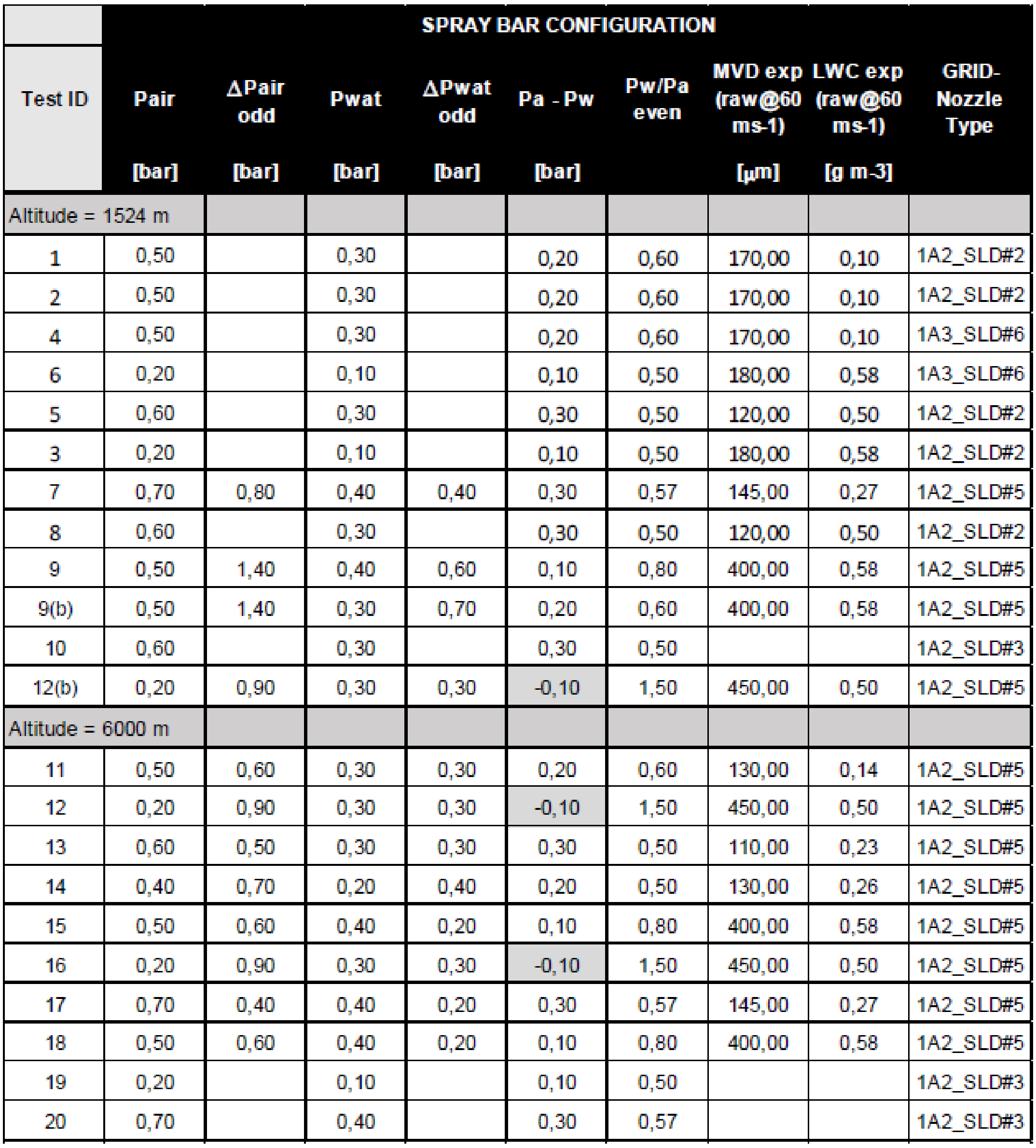

	SPRAY BAR CONFIGURATION								
Test ID	Pair [bar]	ΔPair odd [bar]	Pwat [bar]	ΔPwat odd [bar]	Pa - Pw [bar]	Pw/Pa even	MVD exp (raw@60 ms-1) [μm]	LWC exp (raw@60 ms-1) [g m-3]	GRID-Nozzle Type
Altitude = 1524 m									
1	0,50		0,30		0,20	0,60	170,00	0,10	1A2_SLD#2
2	0,50		0,30		0,20	0,60	170,00	0,10	1A2_SLD#2
4	0,50		0,30		0,20	0,60	170,00	0,10	1A3_SLD#6
6	0,20		0,10		0,10	0,50	180,00	0,58	1A3_SLD#6
5	0,60		0,30		0,30	0,50	120,00	0,50	1A2_SLD#2
3	0,20		0,10		0,10	0,50	180,00	0,58	1A2_SLD#2
7	0,70	0,80	0,40	0,40	0,30	0,57	145,00	0,27	1A2_SLD#5
8	0,60		0,30		0,30	0,50	120,00	0,50	1A2_SLD#2
9	0,50	1,40	0,40	0,60	0,10	0,80	400,00	0,58	1A2_SLD#5
9(b)	0,50	1,40	0,30	0,70	0,20	0,60	400,00	0,58	1A2_SLD#5
10	0,60		0,30		0,30	0,50			1A2_SLD#3
12(b)	0,20	0,90	0,30	0,30	-0,10	1,50	450,00	0,50	1A2_SLD#5
Altitude = 6000 m									
11	0,50	0,60	0,30	0,30	0,20	0,60	130,00	0,14	1A2_SLD#5
12	0,20	0,90	0,30	0,30	-0,10	1,50	450,00	0,50	1A2_SLD#5
13	0,60	0,50	0,30	0,30	0,30	0,50	110,00	0,23	1A2_SLD#5
14	0,40	0,70	0,20	0,40	0,20	0,50	130,00	0,26	1A2_SLD#5
15	0,50	0,60	0,40	0,20	0,10	0,80	400,00	0,58	1A2_SLD#5
16	0,20	0,90	0,30	0,30	-0,10	1,50	450,00	0,50	1A2_SLD#5
17	0,70	0,40	0,40	0,20	0,30	0,57	145,00	0,27	1A2_SLD#5
18	0,50	0,60	0,40	0,20	0,10	0,80	400,00	0,58	1A2_SLD#5
19	0,20		0,10		0,10	0,50			1A2_SLD#3
20	0,70		0,40		0,30	0,57			1A2_SLD#3

Table 10: CIRA-IWT cloud conditions at 45 m/s and Static Air Temperature =-18°C, Total Air Temperature =-17°C

A very low liquid water content (LWC) combined with large droplet size reduced dramatically the probability to have a droplet inside the optical control volume during the camera exposure time. Accordingly, it was not possible to directly record a classical global rainbow signal. Therefore, the real-time image processing software to measure the temperature of the drops cannot be directly used.

Consequently, additional steps must be added in the measurement strategy by:

a) Recording a maximum of images with a short exposure time of about 0.2-0.4 second (this exposure time was selected to maximize the probability of a large droplet being present inside the control volume and simultaneously minimize the parasitic light)
b) Selecting the recorded image where the scattered light can be assumed mainly due to a large droplet.
c) Reconstructing a global rainbow by summing these selected images
d) Processing the numerically reconstructed global rainbow as classically with our processing code based on Nussenzveig [9] [10] theory to describe the scattered light, combined with NNLS and minimisation to extract the mean refractive index.

Due to the above issues, not only the recorded rainbow signals from spherical droplet have been recorded but also the recorded images from deformed droplets, from noise, from the droplet outside of the control volume and etc,. Further data raw treatment was necessary to select the images from which information could be extracted with sufficient confidence. The data processing and analysis procedure have been reported in the project deliverable D4.3 [11].

Figure 63 shows the droplet size and temperature measurements using GRT-Mini for different cloud conditions in CIRA-IWT (Table 10). The measurements were carried out with an airspeed equal to 45m/s and a static air temperature equal to -18°C. The results highlight that, for some conditions, the droplet temperature is slightly higher than the air temperature. However, for a homogenous comparison between the conditions, it is necessary to have the same large number of validated individual images for each case, which was difficult to achieve in CIRA-IWT due to the low LWCs observed.

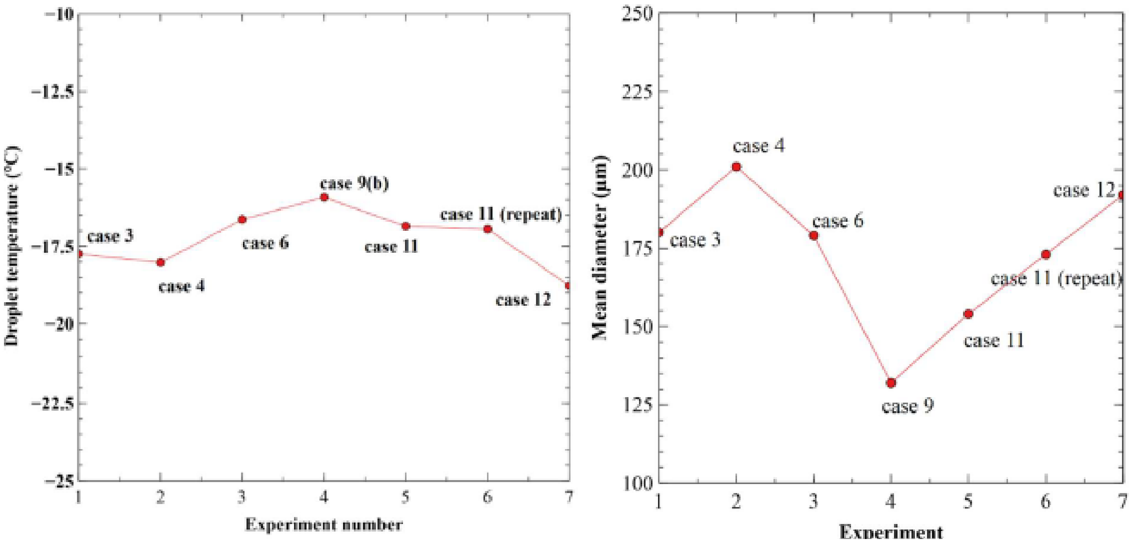

Figure 63: SLD characterization by GRT: average droplet temperature (left) and average droplet diameter (right).

6 Conclusion

The performed measurements, investigations and calibrations have shown that the RTA IWT can produce Appendix O conditions (FZDZ MVD < 40 µm, FZDZ MVD > 40 µm and FZRA MVD > 40 µm) close to the requirements. The main limitations are the relatively high water contents which are required to match the bimodal PSDs in FZDZ and FZRA. This also limits the variability of the producible conditions as the LWC is mainly influenced by the test section airspeed. Ice accretion tests and droplet temperature measurements have shown that the large droplets are sufficiently supercooled at temperatures of colder than -5°C. Further testing is required to investigate if that is still the case at warmer temperatures.

A few test campaigns with FZDZ and FZRA conditions have already been performed and further validation and testing is planned in upcoming research projects. Especially the FZRA setup is still in a prototype stage and needs further improvement to be more practical in a testing environment.

The CIRA-IWT measurements were limited to the FZDZ conditions for some of the possible spray bar system configurations. The results show that low LWC can be achievable in a wide range of the requested envelopes. Nevertheless, more PSD measurements must be collected to better assess the particle spectrum variability at the requested MVD for both FZDZ envelopes (FZDZ MVD < 40 µm, FZDZ MVD > 40 µm and FZRA MVD > 40 µm). A lack of information on cloud uniformity was another gap influenced by the 2D traverse mechanism issue during the last part of the CIRA-IWT calibration slot. To resolve these gaps, within the funded CIRA-ProRA program (Italian Aerospace Research Program), the CIRA-IWT calibration activity will be completed in 2024 also to extend the measurements to different airspeeds and pressure altitudes.

7 References

[1] Cober, S. G., and G. A. Isaac, 2011: “Characterization of Aircraft Icing Environments with Supercooled Large Drops for Application to Commercial Aircraft Certification,” *Journal of Applied Meteorology and Climatology*, Volume 51, pp.265-284, https://doi.org/10.1175/JAMC-D-11-022.1

[2] Federal Aviation Administration FAA, 2009: “Data and Analysis for the Development of an Engineering Standard for Supercooled Large Drop Conditions”, DOT/FAA/AR-09/10, National Technical Information Services (NTIS), Springfield, Virginia 22161

[3] Wierzba, A., “Deformation and breakup of liquid drops in a gas stream at nearly critical Weber numbers,” Experiments in Fluids Vol. 9, pp. 59-64, 1990

[4] King, M.C., Bachalo, W.D., Bell, D. and King-Steen, L.E., “Weber Number Tests in the NASA Icing Research Tunnel”, AIAA

[5] Clift, R., Grace, J. R., and Weber, M. E., Bubbles, Drops and Particles, Dover Publications, Inc., Mineola, 2005

[6] Salman, A. D., and Verba, A., “New Approximate Equations to Estimate the Drag Coefficient of Different Particles of Regular Shape,” Periodica Polytechnica of the Technical University Budapest - Chemical Engineering, Vol. 32,1988

[7] Fallast, A., Rapf, A.R., Tramposch, A. et al. “Kinetic and thermal simulation of water droplets in icing wind tunnels”. CEAS Aeronautical Journal 13, pp. 181–198 (2022). https://doi.org/10.1007/s13272-021-00558-y

[8] Esposito, B., Orchard, D., Lucke, J., Nichman, L. et al., "Comparability of Hot-Wire Estimates of Liquid Water Content in SLD Conditions," SAE Technical Paper 2023-01-1423, 2023, https://doi.org/10.4271/2023-01-1423.

[9] H. Nussenzveig, «High-frequency scattering by a transparent sphere. I. Direct reflection and transmission, Journal of mathematical physics, pp. 82-124, 1969.

[10] H. Nussenzveig, «High-frequency scattering by a transparent sphere. II. Theory of the rainbow and the glory,» Journal of mathematical physics, pp. 125-176, 1969.

[11] Deliverable D4.3, “Report on the review, assessment and selection of instrumentation/model for droplet temperature measurement”